LAWRENCE
LIVERMORE
NATIONAL
LABORATORY

UCRL-TH-236276

A RANS/DES Numerical Procedure for Axisymmetric Flows with and without Strong Rotation

A. J. Andrade

November 7, 2007

Disclaimer

This work performed under the auspices of the U.S. Department of Energy by Lawrence Livermore National Laboratory under Contract DE-AC52-07NA27344.

A RANS/DES Numerical Procedure for Axisymmetric Flows
with and without Strong Rotation

By

ANDREW JACOB ANDRADE

B.S. (University of California, Davis) 2006

THESIS

Submitted in partial satisfaction of the requirements for the degree of

MASTER OF SCIENCE

in

Mechanical and Aeronautical Engineering

in the

OFFICE OF GRADUATE STUDIES

of the

UNIVERSITY OF CALIFORNIA

DAVIS

Approved:

_____

_____

_____

Committee in Charge

2007

Acknowledgments

While obtaining a degree in higher education there have been only a few moments of reflection where I have been able to grasp the wealth of accomplishments I have achieved and at the same time been able to thank all those who have supported me through the years. With the culmination of my masters I would like to acknowledge and express my deepest gratitude to everyone that has been apart of my life, because my family, friends, professors, and colleagues have shaped who I am as a person and without their collective influence I would not be where I am today. I would also like to personally thank the following people for their predominant role in my life.

First and foremost I would like to thank my family, Roxine, Al, and Rebecca, for their support over the years in good times and bad. Family has shown me that success is obtained through achieving ones own personal goals, not the goals desired by others, because only I can determine what makes my life complete.

Next, I would like to thank my advisor, Professor Roger Davis, for his inexhaustible patience and overwhelming support. My decision to further my education was in large part due to your charismatic approach to assisting students and how you bestow a level of professional equality upon students. In a similar light, I would like to thank my high school calculus teacher, Steve Piekarski, for his recognition and encouragement of my academic abilities at a critical stage in life.

Last, I would like acknowledge my friends that have helped me through school and life. Sam Abeyta and Scott Brisbin have shown me not only how to be a good student but how to be a good man, husband, and father. William Logan has shown me how to do what is necessary and what is right, to obtain what I desire academically and personally.

Again, thanks to all those who have inspired and encouraged me throughout the years.

Table of Contents

Table of Figures

Table of Equations

Nomenclature

E	=	total energy
H	=	total enthalpy
h_t	=	total specific enthalpy
h	=	static enthalpy
I	=	rothalpy
k	=	turbulent kinetic energy
ρ	=	density
p	=	pressure
Pr	=	Prandtl number
Pr_t	=	turbulent Prandtl number
S_{ij}	=	mean strain-rate tensor
u	=	axial velocity component
$\hat{u}$	=	internal energy
v	=	radial velocity component
V	=	velocity magnitude
μ	=	coefficient of viscosity
μ_τ	=	turbulent coefficient of viscosity
w	=	tangential velocity component
ω	=	turbulent dissipation rate divided by turbulent kinetic energy
Ω	=	rotational velocity about specified axis of rotation (rads/s)
$\hat{\tau}_{ij}$	=	total viscous stress tensor
τ_{ij}	=	shear stress component
t	=	time
τ	=	pseudo-time

Abstract

A RANS/DES numerical procedure with an extended Lax-Wendroff control-volume scheme and turbulence model is described for the accurate simulation of internal/external axisymmetric flow with and without strong rotation. This new procedure is an extension, from Cartesian to cylindrical coordinates, of 1) a second order accurate multi-grid, control-volume integration scheme, and 2) a k-ω turbulence model. This paper outlines both the axisymmetric corrections to the mentioned numerical schemes and the developments of techniques pertaining to numerical dissipation, multi-block connectivity, parallelization, etc. Furthermore, analytical and experimental case studies are presented to demonstrate accuracy and computational efficiency. Notes are also made toward numerical stability of highly rotational flows.

1 Introduction

Stable numerical schemes for the solution of the cylindrical Reynolds-Averaged Navier-Stokes (RANS) equations with strong rotational source terms are sparse in number and inadequately researched, particularly in the areas of stability criterion, numerical efficiency, and general applicability. Rotational flows are the basis on which a majority of turbomachinery does work. In general, radial diffusion resultant of volume expansion and compression due to Coriolis and centrifugal forces, allows turbomachinery to manipulate fluid properties and thereby extract or utilize fluid energy. This simple illustration conceals the complexity of rotational flow though, which is often a complex shear flow that results from rotational effects and flow curvature[1]. Additionally, the rotational effects distribute turbulent energy thereby, under strong rotation, significantly altering the mean flow by affecting the Reynolds stress terms[1], even though terms, such as those pertaining to Coriolis forces, do not explicitly enter the turbulence equations. Furthermore, rotating systems with flow protruding bodies or even high-speed radial compression systems, such as gas centrifuges, introduce stability issues between secondary flow regions and the main shear flow[2]. In general, these complexities are often a stringent test of numerical stability and require sufficiently accurate initial conditions and highly refined grids to resolve the interaction between the boundary layer and mean shear flow.

In addition to the complexities of the flow physics, rotational flows are typically generated by fully enclosed rotating surfaces which often prevent the acquisition of experimental data that is required for sufficient boundary and initial conditions. Furthermore, highly rotational flows, such as those within gaseous centrifuges, can generate extreme environments such that current numerical methods are unable to resolve the complex flow physics. In particular, high rotation rates can generate regions of rarefied gas – defined by low-densities and Knudsen number at or above unity – in which the Navier-Stokes equations are inadequate in representing the non-continuum fluid mechanics. In such cases as described, more accurate simplifications of the Boltzmann equations, such as the Burnett equations, must be coupled with the Navier-Stokes equations to span the regions of continuum and non-continuum gas. Correspondingly, the ability

to obtain sufficient experimental flow characteristics in high rotation flow is impractical if not unfeasible due to the fact that any use of measurement devices will alter the flow dynamics.

Due to the complexities of rotating flows, particularly in flow systems which violate the continuum assumption, numerical analysis has been limited to theoretical studies in which equations of the general flow physics and tacit assumptions have provided analytical equations for calculating the performance of simple flows[3]. Unfortunately, these methods give no insight to the true internal flow characteristics and thus numerical application to design and general understanding has been limited. Significant work by Tsunetoshi Kai[3] though, has shown promise with the axi-symmetric solution of the Navier-Stokes equations for the analysis of flows with and without strong rotation. Kai was able to solve the N-S equations along with the Burnett equations for accurate analysis of gas centrifugation at high rotation, where centerline flow becomes rarefied, along with inflow/outflow and thermal boundary gradients[3]. To improve on the numerical procedures developed by Kai, a general, highly stable numerical scheme with limited constraints and applicability to flows with and without strong rotation is required for the intensions of design analysis and gaining an improved understanding of complex rotating flows.

For the design and analysis of rotating machinery with and without strong rotation, or in general any axisymmetric system, a numerical procedure for the solution of the axi-symmetric Navier-Stokes equations in their entirety, with the advantages of multi-grid acceleration and turbulent modeling accuracy is necessary. Thus extensions to cylindrical coordinates of both the Ni integration method (an extension of the Lax-Wendroff scheme) and the Wilcox k-ω turbulence model are outlined, and validation with analytical and experimental case studies is presented. Additionally, a brief outline and initial solution to basic rotational stability issues will be addressed. Moreover, an accurate and computationally efficient axisymmetric scheme applicable for flows with and without strong rotation is presented.

2 Governing Equations

The axisymmetric unsteady, Favre-averaged governing flow-field equations for an ideal, compressible gas in a right-handed, cylindrical coordinate system using relative-frame primary variables can be written in strong form as:

Equation 1: Conservation of Mass (strong form)

$$\frac{\partial \rho}{\partial t} = -\frac{\partial(\rho u)}{\partial z} - \frac{1}{r}\frac{\partial(\rho v r)}{\partial r}$$

Equation 2: Axial Momentum (strong form)

$$\frac{\partial \rho u}{\partial t} = \begin{bmatrix} -\dfrac{\partial(\rho u u + p)}{\partial z} - \dfrac{1}{r}\dfrac{\partial(\rho v u r)}{\partial r} \\ +\dfrac{\partial(\tau_{zz})}{\partial z} + \dfrac{1}{r}\dfrac{\partial(\tau_{zr} r)}{\partial r} \end{bmatrix}$$

Equation 3: Radial Momentum (strong form)

$$\frac{\partial \rho v}{\partial t} = \begin{bmatrix} -\dfrac{\partial(\rho u v)}{\partial z} - \dfrac{1}{r}\dfrac{\partial(\rho v v r + p r)}{\partial r} \\ +\dfrac{\partial(\tau_{rz})}{\partial z} + \dfrac{1}{r}\dfrac{\partial(\tau_{rr} r)}{\partial r} \\ +\dfrac{p + \rho w^2}{r} - \overline{Sm}_r \end{bmatrix}$$

Equation 4: Azimuthal (Tangential) Momentum (strong form)

$$\frac{\partial \rho w}{\partial t} = \begin{bmatrix} -\dfrac{\partial(\rho u w)}{\partial z} - \dfrac{1}{r}\dfrac{\partial(\rho v w r)}{\partial r} \\ +\dfrac{\partial(\tau_{\theta z})}{\partial z} + \dfrac{1}{r}\dfrac{\partial(\tau_{\theta r} r)}{\partial r} + \dfrac{\tau_{\theta r}}{r} \\ -\dfrac{\rho v w}{r} - \overline{Sm}_\theta \end{bmatrix}$$

Equation 5: Conservation of Energy (strong form)

$$\frac{\partial E}{\partial t} = \begin{bmatrix} -\dfrac{\partial(\rho I u)}{\partial z} - \dfrac{1}{r}\dfrac{\partial(\rho I v r)}{\partial r} \\ +\dfrac{\partial(\tau_{hz})}{\partial z} + \dfrac{1}{r}\dfrac{\partial(\tau_{hr} r)}{\partial r} \end{bmatrix}$$

Assuming Newtonian fluids, the viscous stress terms are related to the viscosity and strain rates as follows:

Equation 6: Newtonian Stresses

$$\tau_{zz} = \mu\left[\frac{4}{3}\frac{\partial u}{\partial z} - \frac{2}{3}\frac{1}{r}\frac{\partial v r}{\partial r}\right] \qquad \tau_{z\theta} = \mu\left[\frac{\partial w}{\partial z}\right]$$

$$\tau_{rr} = \mu\left[\frac{4}{3}\frac{1}{r}\frac{\partial v r}{\partial r} - \frac{2}{3}\frac{\partial u}{\partial z} - 2\frac{v}{r}\right] \qquad \tau_{r\theta} = \mu\left[\frac{1}{r}\frac{\partial w r}{\partial r} - 2\frac{w}{r}\right]$$

$$\tau_{zr} = \mu\left[\frac{\partial u}{\partial r} + \frac{\partial v}{\partial z}\right]$$

Equation 7: Conduction and Viscous Work

$$\tau_{hz} = \left[\frac{\mu}{\Pr} \frac{\partial h}{\partial z} + u\tau_{zz} + v\tau_{zr} + w\tau_{z\theta} \right]$$
$$\tau_{hr} = \left[\frac{\mu r}{\Pr} \frac{\partial h}{\partial r} + ur\tau_{zr} + vr\tau_{rr} + wr\tau_{r\theta} \right]$$

Using Gauss's Theorem, the Navier-Stokes equations can be written in integral form, which is more conducive to numerical solution and representative of the numerical schemes to be outlined.

Equation 8: Conservation of Mass (integral form)

$$\int \frac{\partial \rho}{\partial t} dV_{ol} = -\oint (\rho u) r d\theta dr + \oint (\rho v) r d\theta dz$$

Equation 9: Axial Momentum (integral form)

$$\int \frac{\partial \rho u}{\partial t} dV_{ol} = \begin{bmatrix} -\oint (\rho uu + p) r d\theta dr + \oint (\rho vu) r d\theta dz \\ +\oint (\tau_{zz}) r d\theta dr - \oint (\tau_{zr}) r d\theta dz \end{bmatrix}$$

Equation 10: Radial Momentum (integral form)

$$\int \frac{\partial \rho v}{\partial t} dV_{ol} = \begin{bmatrix} -\oint (\rho uv) r d\theta dr + \oint (\rho vv + p) r d\theta dz \\ +\oint (\tau_{rz}) r d\theta dr - \oint (\tau_{rr}) r d\theta dz \\ +\int \frac{(p + \rho w^2)}{r} dV_{ol} - \int \overline{Sm}_r dV_{ol} \end{bmatrix}$$

Equation 11: Azimuthal Momentum (integral form)

$$\int \frac{\partial \rho w}{\partial t} dV_{ol} = \begin{bmatrix} -\oint (\rho uw) r d\theta dr + \oint (\rho vw) r d\theta dz \\ +\oint (\tau_{\theta z}) r d\theta dr - \oint (\tau_{\theta r}) r d\theta dz + \int \frac{\tau_{\theta r}}{r} dV_{ol} \\ -\int \frac{\rho vw}{r} dV_{ol} - \int \overline{Sm}_\theta dV_{ol} \end{bmatrix}$$

Equation 12: Conservation of Energy (integral form)

$$\int \frac{\partial E}{\partial t} dV_{ol} = \begin{bmatrix} -\oint (\rho Iu) r d\theta dr + \oint (\rho Iv) r d\theta dx \\ +\oint (\tau_{hz}) r d\theta dr - \oint (\tau_{hr}) r d\theta dx \end{bmatrix}$$

Equation 13: Total Energy

$$E = \rho \hat{u} + \frac{\rho V^2}{2} - \frac{1}{2} \rho (\Omega r)^2$$

Equation 14: Rothalpy

$$I = H - \frac{1}{2} (\Omega r)^2 = \frac{E + P}{\rho}$$

Equation 15: Enthalpy

$$h = H - \frac{V^2}{2} = \hat{u} + \frac{P}{\rho}$$

Equation 16: Total Viscous Stress Tensor

$$\hat{\tau}_{ij} = (\mu + \mu_t) S_{ij}$$

Equation 17: Mean Strain Rate Tensor

$$S_{ij} = \left(\nabla_j u_i + \nabla_i u_j \right) - \frac{2}{3} \nabla_k u_k \delta_{ij}$$

Equation 18: Cylindrical Gradient Operators

$$\nabla = \frac{\partial}{\partial r} + \frac{1}{r}\frac{\partial}{\partial \theta} + \frac{\partial}{\partial z},\ \nabla_z = \frac{\partial}{\partial z},\ \nabla_r = \frac{\partial}{\partial r},\ \nabla_\theta = \frac{1}{r}\frac{\partial}{\partial \theta}$$

For axisymmetric flow with rotation, the body-force vector, S_{mi}, in the momentum equations, Eqs. 9 – 11, represents the relative Coriolis and centripetal effects in a rotating (non-inertial) reference frame. Thus, considering steady rotation, the body-force vector is defined as:

Equation 19: Momentum Source Vector

$$\overline{Sm}_i = -2\rho\left(\overline{\Omega} \times V\right) - \rho\overline{\Omega} \times \left(\overline{\Omega} \times \overline{R}\right)$$

Limiting rotation to around the z-axis only and defining an arbitrary rotational speed, Ω, the momentum source term vector becomes:

Equation 20: Momentum Source Vector

$$\overline{Sm}_i = \begin{bmatrix} 0 \\ 2\rho\Omega w + \rho\Omega^2 r \\ -2\rho\Omega v \end{bmatrix} \begin{matrix} (\text{z - direction}) \\ (\text{r - direction}) \\ (\theta\text{ - direction}) \end{matrix}$$

Additional governing equations as developed by Wilcox[4] for the transport of turbulent kinetic energy and dissipation rate in regions of the flow where the computational grid or global time-step size are unable to resolve the turbulent eddies can be written in integral form as:

Equation 21: Turbulent Kinetic Energy Transport

$$\begin{aligned} \int \frac{\partial(\rho k)}{\partial t} dV_{ol} = &-\oint (\rho u k) r d\theta dr + \oint (\rho v k) r d\theta dz \\ &+ \int \left[\left(\tau_{ij} - \frac{2}{3}\rho k \delta_{ij} \right) \nabla_j u_i \right] dV_{ol} - \int \left(\beta^* \rho k \omega \right) dV_{ol} \\ &+ \oint \left[\left(\mu + \sigma^* \frac{\rho k}{\omega} \right) \frac{\partial k}{\partial z} \right] r d\theta dz - \oint \left[\left(\mu + \sigma^* \frac{\rho k}{\omega} \right) \frac{\partial k}{\partial r} \right] r d\theta dr \end{aligned}$$

Equation 22: Turbulent Dissipation Transport

$$\begin{aligned} \int \frac{\partial(\rho \omega)}{\partial t} dV_{ol} = &-\oint (\rho u \omega) r d\theta dr + \oint (\rho v \omega) r d\theta dz \\ &+ \int \left[\frac{\gamma \omega}{k} \left(\tau_{ij} - \frac{2}{3}\rho k \delta_{ij} \right) \nabla_j u_i \right] dV_{ol} - \int \left(\beta \rho \omega^2 \right) dV_{ol} \\ &+ \oint \left[\left(\mu + \sigma^* \frac{\rho k}{\omega} \right) \frac{\partial \omega}{\partial z} \right] r d\theta dz - \oint \left[\left(\mu + \sigma^* \frac{\rho k}{\omega} \right) \frac{\partial \omega}{\partial r} \right] r d\theta dr \end{aligned}$$

Equation 23: Sub-Grid Coefficient of Turbulent Viscosity

$$\mu_t = \frac{\rho k}{\omega}$$

In regions of the flow where the larger-scale eddies can be resolved with the computational grid, techniques borrowed from large-eddy simulation are used to represent the viscous shear and turbulent viscosity. The large-eddy sub-grid model described by Smagorinsky[5] is modified according to the detached-eddy considerations described by Strelets[6] and Bush and Mani[7] in which the turbulent viscosity is determined with

Equation 24: Large-Eddy Coefficient of Turbulent Viscosity

$$\mu_t = \rho l_{le} \sqrt{k}$$

where l_{le} is an eddy length scale proportional to the grid/time-step filter width, Δ. In addition, the dissipation term, $\beta^* \rho k \omega$, of the turbulent kinetic energy transport equation (Eq. 21) is limited by the eddy length scale, l_{le}, according to:

Equation 25: Kinetic Energy Dissipation

$$\beta^* \rho k \omega = \beta^* \rho k \max\left(\omega, \frac{\sqrt{k}}{C_{des}\Delta}\right)$$

where C_{des} is a proportionality coefficient.

3 General Second-Order Finite Volume Integration Method (Ni Scheme)

In general, the two-dimensional Navier-Stokes equations can be solved sufficiently easy and accurately by a Lax-Wendroff integration scheme. To improve computation time, memory allocation, programming difficulty, and applicability to multi-grid techniques, Ni[9] extended the Lax-Wendroff scheme to perform the first and second order temporal integrations in a single cell-centered distributive method. Ni's distributive integration method[9] in a two-dimensional Cartesian system writes the general unsteady Euler equations as:

Equation 26: General Two-Dimensional Euler Equations

$$\frac{\partial U}{\partial t} = -\left[\frac{\partial (F(U))}{\partial x} + \frac{\partial (G(U))}{\partial y}\right]$$

$$U = \begin{bmatrix} \rho \\ \rho u \\ \rho v \\ e \end{bmatrix} \quad F(U) = \begin{bmatrix} \rho u \\ \rho uu + p \\ \rho uv \\ \rho u h_t \end{bmatrix} \quad G(U) = \begin{bmatrix} \rho v \\ \rho vu \\ \rho vv + p \\ \rho v h_t \end{bmatrix}$$

$$h_t = \frac{e+p}{\rho} = \frac{\gamma}{(\gamma-1)}\frac{p}{\rho} + \frac{1}{2}\left(u^2 + v^2\right)$$

For the Ni/Lax-Wendroff scheme, second order accurate temporal integrations are achieved from a Taylor series expansion as follows:

Equation 27: Taylor Series Temporal Expansion

$$\delta U_i^{n+1} = \Delta t\left(\frac{\partial U}{\partial t}\right)_i^n + \frac{\Delta t^2}{2}\left(\frac{\partial^2 U}{\partial t^2}\right)_i^n$$

The first term of the Taylor series expansion, $\partial U/\partial t$, is explicitly the Euler Equations and thus can be solved directly from integration around each numerical cell. The second order temporal terms of the Taylor series though, can be rewritten as follows:

Equation 28: Second Order Temporal Terms

$$\frac{\Delta t^2}{2}\frac{\partial^2 U}{\partial t^2} = \frac{\Delta t}{2}\frac{\partial}{\partial t}\left[\frac{\partial U}{\partial t}\Delta t\right]$$

$$= -\frac{\Delta t}{2}\frac{\partial}{\partial t}\left[\frac{\partial}{\partial x}\left(\frac{\partial F}{\partial t}\Delta t\right) + \frac{\partial}{\partial y}\left(\frac{\partial G}{\partial t}\Delta t\right)\right]$$

$$= -\frac{\Delta t}{2}\frac{\partial}{\partial t}\left[\frac{\partial}{\partial x}\left(\frac{\partial F}{\partial U}\frac{\partial U}{\partial t}\Delta t\right) + \frac{\partial}{\partial y}\left(\frac{\partial G}{\partial U}\frac{\partial U}{\partial t}\Delta t\right)\right]$$

The second order temporal terms consist of the Jacobians, $\partial F/\partial U$ and $\partial G/\partial U$, and the first order temporal terms, $\partial U/\partial t$, thus allowing simultaneous calculation of the first and second order temporal terms. The Jacobians and the first order temporal terms are calculated at cells centers

though, thus requiring the second order integrations to be obtained from a secondary or offset grid that has nodal points defined by the primary grids cell-centered positions. To avoid a secondary grid, Ni decouples the integration of the second order terms into a piecewise integration method, which allows the cell-centered contributions to the nodal changes, δU_i, to be calculated independently of adjoining cells. In other words, the Ni scheme allows the cell-centered contributions of the nodal changes to be calculated inclusively and then distributed to the surrounding nodes where it accumulates with the changes of adjoining cells. The calculations of first and second order temporal terms are shown below for a one-dimensional Cartesian system.

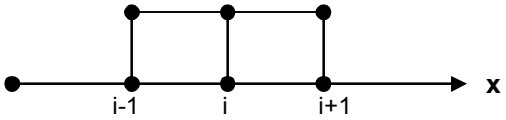

Figure 1: One-Dimensional Control Area

Equation 29: One Dimensional Solution of Temporal Integration

$$\delta U_i = \frac{1}{2}\left[\Delta U_{i-\frac{1}{2}} + \frac{\Delta t}{\Delta x}\left(\frac{\partial F}{\partial U}\right)_{i-\frac{1}{2}} \Delta U_{i-\frac{1}{2}}\right] \quad \leftarrow term1$$

$$+\frac{1}{2}\left[\Delta U_{i+\frac{1}{2}} - \frac{\Delta t}{\Delta x}\left(\frac{\partial F}{\partial U}\right)_{i+\frac{1}{2}} \Delta U_{i+\frac{1}{2}}\right] \quad \leftarrow term2$$

where :

$$\Delta U_{i-\frac{1}{2}} = \left(F_{i-1}^n - F_i^n\right)\frac{\Delta t}{\Delta x}$$

$$\Delta U_{i+\frac{1}{2}} = \left(F_i^n - F_{i+1}^n\right)\frac{\Delta t}{\Delta x}$$

From Equation 29, terms 1 and 2 correspond to the cell-centered first and second order temporal changes distributed from cells i-½ and i+½, respectively, to node i.

Since the Lax-Wendroff procedure is an explicit integration scheme, numerical stability is a function of grid size and wave speed and thus is controlled by the Courant-Friedrichs-Lewi (CFL) condition as follows:

Equation 30: CFL Stability Criteria

$$\Delta t \le \frac{CFL\,\Delta x}{|W|}$$

where W is the wave speed and CFL is the stability number. The wave speed, W, is defined by the maximum of upstream and downstream wave speeds, which for a one-dimensional flow is defined as:

Equation 31: Wave Speed Equation $$W = \max\left|(u+c),(u-c)\right|$$

where c is the speed of sound.

4 Axisymmetric RANS Scheme

For axisymmetric flows, the conservation equations given in Eqs. 8 – 12, 21, and 22 are solved using an extension of the Ni/Lax-Wendroff finite-volume, time-marching scheme as developed by Andrade[8], Ni[9], Dannenhoffer[10], and Davis[11,12]. These techniques are second-order accurate in time and space. A multiple-grid convergence acceleration scheme[3] is used for steady Reynolds-averaged solutions and the inner convergence loop of unsteady simulations of a dual time-step scheme. The first and second-order temporal distribution scheme performs a finite-volume integration of the fluxes around each cell of the domain to obtain the time-rate changes[3] pertaining to the individual cells, as outlined in the previous section. The time dependent corrections at the nodes are thereby determined from "distribution formulas"[9], which are generated from a piecewise decoupling of the finite-volume integrals. This scheme allows temporal changes at each node to be determined by an amalgamation of the changes within adjoined cells, where the cell based contributions to the nodal changes are determined independent of other cells. This technique eliminates the flux determining inclusion of ghost node data from outside of the domain. The following sub-sections will outline the axisymmetric corrections to the finite-volume distribution scheme, described previously, on the Euler equations for simplicity and brevity, but application to both the viscous terms and turbulence equations is identical.

4.1 Axisymmetric Extension of the Ni/Lax-Wendroff First Order Temporal Term Calculation

For an axisymmetric domain, derivation of the cell fluxes must be shown two-dimensionally due to radial volume expansion. The layout of an arbitrary axisymmetric two-dimensional grid, in the z-r plane, is given below in Figure 2.

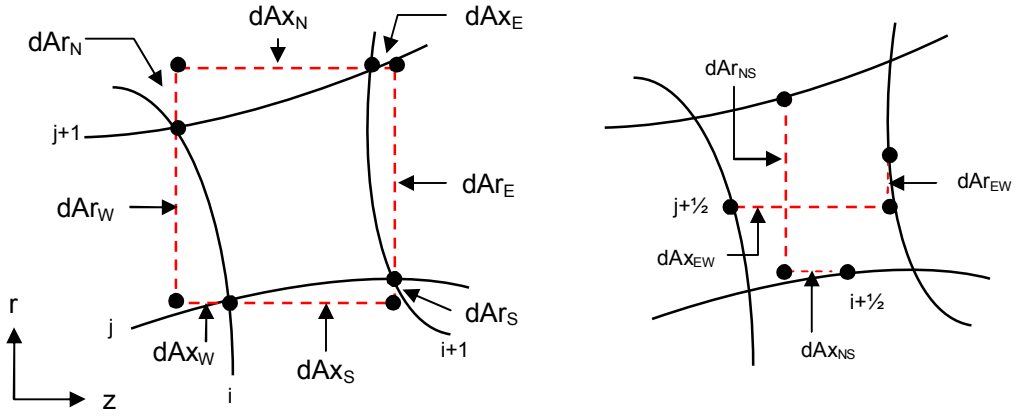

Figure 2: General two-dimensional finite control volume with projected face areas.

The corresponding projected area terms are defined as follows:

Equation 32: General Axisymmetric cell projected finite areas

$$dAr_W = \left(r_{i,j+1} - r_{i,j}\right)\left(r_{i,j+1} + r_{i,j}\right)/2$$
$$dAz_W = \left(z_{i,j+1} - z_{i,j}\right)\left(r_{i,j+1} + r_{i,j}\right)/2$$
$$dAr_E = \left(r_{i+1,j+1} - r_{i+1,j}\right)\left(r_{i+1,j+1} + r_{i+1,j}\right)/2$$
$$dAz_E = \left(z_{i+1,j+1} - z_{i+1,j}\right)\left(r_{i+1,j+1} + r_{i+1,j}\right)/2$$
$$dAr_S = \left(r_{i+1,j} - r_{i,j}\right)\left(r_{i+1,j} + r_{i,j}\right)/2$$
$$dAz_S = \left(z_{i+1,j} - z_{i,j}\right)\left(r_{i+1,j} + r_{i,j}\right)/2$$
$$dAr_N = \left(r_{i+1,j+1} - r_{i,j+1}\right)\left(r_{i+1,j+1} + r_{i,j+1}\right)/2$$
$$dAz_N = \left(z_{i+1,j+1} - z_{i,j+1}\right)\left(r_{i+1,j+1} + r_{i,j+1}\right)/2$$

Equation 33: General Axisymmetric cell-centered finite areas

$$dAr_{NS} = \left(r_{i+\frac{1}{2},j+1} - r_{i+\frac{1}{2},j}\right)\left(r_{i+\frac{1}{2},j+1} + r_{i+\frac{1}{2},j}\right)/2$$
$$dAz_{NS} = \left(z_{i+\frac{1}{2},j+1} - z_{i+\frac{1}{2},j}\right)\left(r_{i+\frac{1}{2},j+1} + r_{i+\frac{1}{2},j}\right)/2$$
$$dAr_{EW} = \left(r_{i,j+\frac{1}{2}} - r_{i+1,j+\frac{1}{2}}\right)\left(r_{i,j+\frac{1}{2}} + r_{i+1,j+\frac{1}{2}}\right)/2$$
$$dAz_{EW} = \left(z_{i,j+\frac{1}{2}} - z_{i+1,j+\frac{1}{2}}\right)\left(r_{i,j+\frac{1}{2}} + r_{i+1,j+\frac{1}{2}}\right)/2$$

As outlined in Section 3, a Taylor series expansion of temporal changes to the independent flow variables is determined by solution of the explicit one-step second-order approximation given

by Equation 27. As for a two-dimensional Cartesian system, the axisymmetric first order temporal approximation pertains to the solution of the Navier-Stokes equations, Eqs. 8 – 12, as explicitly written, which is achieved by control volume integration around each cell to determine the fluxes at the cell centers. For the Euler equations, this is in general obtained as follows:

Equation 34: Axisymmetric Solution of First Order Temporal Terms (Euler Eqs.)

$$\frac{\partial U}{\partial t} = -\frac{\partial (F)}{\partial z} - \frac{1}{r}\frac{\partial (rG)}{\partial r}$$

$$\Delta t \frac{\partial U}{\partial t} = \Delta t \left[-\frac{\partial (F)}{\partial z} - \frac{1}{r}\frac{\partial (rG)}{\partial r} \right]$$

$$\Delta t \left. \frac{\partial U}{\partial t} \right|_c = \frac{\Delta t}{V_{ol}} \left[-\oint (F) r d\theta dr + \oint (G) r d\theta dz \right]$$

$$\Delta U_{cell\ center} = \Delta t \left. \frac{\partial U}{\partial t} \right|_c =$$

$$\frac{\Delta t}{2V_{ol}} \begin{bmatrix} \left(F_{i,j+1} + F_{i,j}\right) dAr_W - \left(F_{i+1,j} + F_{i,j}\right) dAr_S \\ -\left(F_{i+1,j+1} + F_{i+1,j}\right) dAr_E + \left(F_{i,j+1} + F_{i+1,j+1}\right) dAr_N \\ -\left(G_{i,j+1} + G_{i,j}\right) dAz_W + \left(G_{i+1,j} + G_{i,j}\right) dAz_S \\ +\left(G_{i+1,j+1} + G_{i+1,j}\right) dAz_E - \left(G_{i,j+1} + G_{i+1,j+1}\right) dAz_N \end{bmatrix}$$

where F and G are defined as they where in Equation 26. With the cell centered first order temporal changes determined, a distribution method to the surrounding nodes is required to update the nodal flow variables.

4.2 Axisymmetric First Order Temporal Term Distribution

The original derivation of the Ni distribution formulas[9] assumed a uniform grid for a two-dimensional Cartesian system, thus distribution of the first order temporal terms to the cell nodes was one-quarter, or a homogeneous distribution. In systems with strong rotation, accurate resolution of the viscous layers, or more critically the Ekman layers, establishes the near wall grid spacing while accurate pressure propagation and flow convection sets grid spacing in the main flow. Therefore, changes of several orders of magnitude in grid density can exist between the near wall and main flow regions, thus indicating the ineptitude of a uniform grid approximation for an accurate distribution method, especially in axisymmetric configurations. Numerically, when applying the Ni scheme to a stretched grid as shown in Figure 3, the resultant first order term is representative of the offset node, i_{off},j_{off}, presenting an error that can propagate with iterations and will effect the accuracy of steady-state solutions.

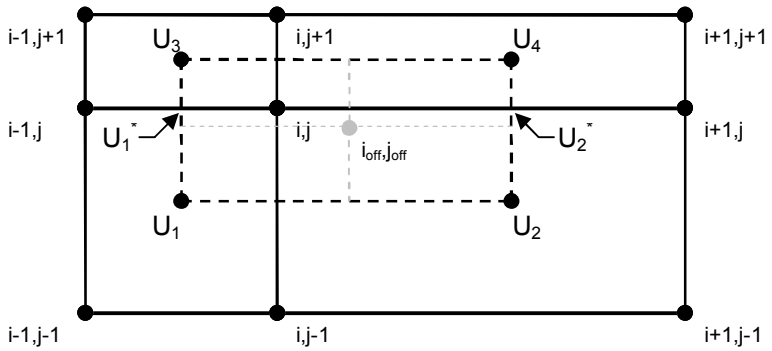

Figure 3: Axisymmetric Temporal Distribution Layout 1

Though increasing grid density reduces the distribution error, accounting for stretched grids will uniformly reduce error. Additionally, by accounting for radial volume expansion for axisymmetric flows, the distribution of the first order temporal changes will produce more accurate nodal results, thus providing a more viable and general numerical scheme with increased accuracy and improved convergence. The inclusion of grid stretching and radial volume expansion is obtained by performing a volume weighted three-step linear interpolation of the first order temporal changes surrounding each node.

4.2.1 Volume Weighted Three-Step Interpolation

Referring to Figure 3, where $U_{1\text{-}4}$ represent first order temporal changes at the cell centers (i.e. $U_1 = U_{i\text{-}½,j\text{-}½}$, etc.), the three-step interpolation consist of linear interpolations between $U_1|U_3$, $U_2|U_4$, and the products of the resulting two interpolations. The result is the same as a volume-weighted bi-linear interpolation of changes from cell-centered values at 1,2,3,4 to node i,j. Since the flow variables have extensive properties, the cell-centered and nodal first order temporal changes are multiplied by their corresponding volumes to weight their respective interpolation influence. This can be done as follows:

Equation 35: Interpolation 1

$$\frac{U_3 V_{i-\frac{1}{2},j+\frac{1}{2}} - U_1^* V_{i-\frac{1}{2},j}}{r_{i-\frac{1}{2},j+\frac{1}{2}} - r_{i-\frac{1}{2},j}} = \frac{U_1^* V_{i-\frac{1}{2},j} - U_1 V_{i-\frac{1}{2},j-\frac{1}{2}}}{r_{i-\frac{1}{2},j} - r_{i-\frac{1}{2},j-\frac{1}{2}}}$$

$$U_1^* = \frac{1}{V_{i-\frac{1}{2},j}} \left[\frac{U_1 V_{i-\frac{1}{2},j-\frac{1}{2}} + U_3 V_{i-\frac{1}{2},j+\frac{1}{2}} \left(\frac{r_{i-\frac{1}{2},j} - r_{i-\frac{1}{2},j-\frac{1}{2}}}{r_{i-\frac{1}{2},j+\frac{1}{2}} - r_{i-\frac{1}{2},j}} \right)}{1 + \left(\frac{r_{i-\frac{1}{2},j} - r_{i-\frac{1}{2},j-\frac{1}{2}}}{r_{i-\frac{1}{2},j+\frac{1}{2}} - r_{i-\frac{1}{2},j}} \right)} \right]$$

Equation 36: Interpolation 2

$$\frac{U_4 V_{i+\frac{1}{2},j+\frac{1}{2}} - U_2^* V_{i+\frac{1}{2},j}}{r_{i+\frac{1}{2},j+\frac{1}{2}} - r_{i+\frac{1}{2},j}} = \frac{U_2^* V_{i+\frac{1}{2},j} - U_2 V_{i+\frac{1}{2},j-\frac{1}{2}}}{r_{i+\frac{1}{2},j} - r_{i+\frac{1}{2},j-\frac{1}{2}}}$$

$$U_2^* = \frac{1}{V_{i+\frac{1}{2},j}} \left[\frac{U_2 V_{i+\frac{1}{2},j-\frac{1}{2}} + U_4 V_{i+\frac{1}{2},j+\frac{1}{2}} \left(\frac{r_{i+\frac{1}{2},j} - r_{i+\frac{1}{2},j-\frac{1}{2}}}{r_{i+\frac{1}{2},j+\frac{1}{2}} - r_{i+\frac{1}{2},j}} \right)}{1 + \left(\frac{r_{i+\frac{1}{2},j} - r_{i+\frac{1}{2},j-\frac{1}{2}}}{r_{i+\frac{1}{2},j+\frac{1}{2}} - r_{i+\frac{1}{2},j}} \right)} \right]$$

Equation 37: Interpolation 3

$$\frac{U_2^* V_{i+\frac{1}{2},j} - U_{i,j} V_{i,j}}{z_{i+\frac{1}{2},j} - z_{i,j}} = \frac{U_{i,j} V_{i,j} - U_1^* V_{i-\frac{1}{2},j}}{z_{i,j} - z_{i-\frac{1}{2},j}}$$

$$U_{i,j} = \frac{1}{V_{i,j}} \left[\frac{U_1^* V_{i-\frac{1}{2},j} + U_2^* V_{i+\frac{1}{2},j} \left(\frac{z_{i,j} - z_{i-\frac{1}{2},j}}{z_{i+\frac{1}{2},j} - z_{i,j}} \right)}{1 + \left(\frac{z_{i,j} - z_{i-\frac{1}{2},j}}{z_{i+\frac{1}{2},j} - z_{i,j}} \right)} \right]$$

At this point, the products of the first two interpolation steps are substituted into Equation 37 and simplified to present a more workable equation.

Equation 38: Accumulation and Simplification of Interpolation steps

$$U_{i,j} = \frac{\left[\begin{array}{l} \left[\frac{U_1 V_{i-\frac{1}{2},j-\frac{1}{2}}\left(r_{i-\frac{1}{2},j+\frac{1}{2}} - r_{i-\frac{1}{2},j}\right)}{r_{i-\frac{1}{2},j+\frac{1}{2}} - r_{i-\frac{1}{2},j} + r_{i-\frac{1}{2},j} - r_{i-\frac{1}{2},j-\frac{1}{2}}}\right]\left(z_{i+\frac{1}{2},j} - z_{i,j}\right) + \\ \left[\frac{U_2 V_{i+\frac{1}{2},j-\frac{1}{2}}\left(r_{i+\frac{1}{2},j+\frac{1}{2}} - r_{i+\frac{1}{2},j}\right)}{r_{i+\frac{1}{2},j+\frac{1}{2}} - r_{i+\frac{1}{2},j} + r_{i+\frac{1}{2},j} - r_{i+\frac{1}{2},j-\frac{1}{2}}}\right]\left(z_{i,j} - z_{i-\frac{1}{2},j}\right) + \\ \left[\frac{U_3 V_{i-\frac{1}{2},j+\frac{1}{2}}\left(r_{i-\frac{1}{2},j} - r_{i-\frac{1}{2},j-\frac{1}{2}}\right)}{r_{i-\frac{1}{2},j+\frac{1}{2}} - r_{i-\frac{1}{2},j} + r_{i-\frac{1}{2},j} - r_{i-\frac{1}{2},j-\frac{1}{2}}}\right]\left(z_{i+\frac{1}{2},j} - z_{i,j}\right) + \\ \left[\frac{U_4 V_{i+\frac{1}{2},j+\frac{1}{2}}\left(r_{i+\frac{1}{2},j} - r_{i+\frac{1}{2},j-\frac{1}{2}}\right)}{r_{i+\frac{1}{2},j+\frac{1}{2}} - r_{i+\frac{1}{2},j} + r_{i+\frac{1}{2},j} - r_{i+\frac{1}{2},j-\frac{1}{2}}}\right]\left(z_{i,j} - z_{i-\frac{1}{2},j}\right) \end{array}\right]}{V_{i,j}\left[z_{i+\frac{1}{2},j} - z_{i,j} + z_{i,j} - z_{i-\frac{1}{2},j}\right]}$$

Through simplification, Equation 38 shows that the temporal contributions of a node's surrounding cells are coupled through a grid dependency, which if simplified, cancels out for two-dimensional Cartesian systems assuming a uniform grid; matching Ni's scheme[9]. Referring again to Figure 3 though, further simplification to Equation 38 can be made by relating the product of length terms, Δz and Δr, to cell based area terms. The resulting equation is:

Equation 39: Distributed First Order Temporal Equation

$$U_{i,j} = \frac{1}{4}\left[\begin{array}{l} \left[U_1 \frac{V_{i-\frac{1}{2},j-\frac{1}{2}}}{V_{i,j}} \frac{A_{i+\frac{1}{2},j+\frac{1}{2}}}{A_{i,j}}\right] + \left[U_2 \frac{V_{i+\frac{1}{2},j-\frac{1}{2}}}{V_{i,j}} \frac{A_{i-\frac{1}{2},j+\frac{1}{2}}}{A_{i,j}}\right] + \\ \left[U_3 \frac{V_{i-\frac{1}{2},j+\frac{1}{2}}}{V_{i,j}} \frac{A_{i+\frac{1}{2},j-\frac{1}{2}}}{A_{i,j}}\right] + \left[U_4 \frac{V_{i+\frac{1}{2},j+\frac{1}{2}}}{V_{i,j}} \frac{A_{i-\frac{1}{2},j-\frac{1}{2}}}{A_{i,j}}\right] \end{array}\right]$$

At this point, physical interpretation of the resulting distribution equation can be made, but first the equation will be decoupled into cell based contributions, similar to the Ni distribution method[9].

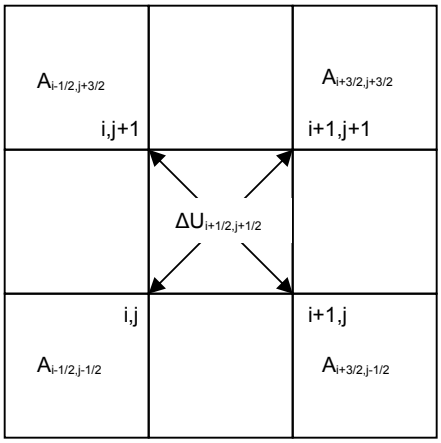

Figure 4: Axisymmetric Temporal Distribution Layout 2

Referring to Figure 4, the decoupling of Equation 39 to generate a piecewise correction to the Ni first order temporal term distribution scheme produced the following terms as cell based contributions to the nodal flow properties:

First Order Temporal Distribution to Node i+1,j+1:

$$\Delta U_{i+\frac{1}{2},j+\frac{1}{2}}\left[\frac{1}{4}\left(\frac{V_{i+\frac{1}{2},j+\frac{1}{2}}}{V_{i+1,j+1}}\right)\frac{A_{i+\frac{3}{2},j+\frac{3}{2}}}{A_{i+1,j+1}}\right]$$

First Order Temporal Distribution to Node i+1,j:

$$\Delta U_{i+\frac{1}{2},j+\frac{1}{2}}\left[\frac{1}{4}\left(\frac{V_{i+\frac{1}{2},j+\frac{1}{2}}}{V_{i+1,j}}\right)\frac{A_{i+\frac{3}{2},j-\frac{1}{2}}}{A_{i+1,j}}\right]$$

First Order Temporal Distribution to Node i,j:

$$\Delta U_{i+\frac{1}{2},j+\frac{1}{2}}\left[\frac{1}{4}\left(\frac{V_{i+\frac{1}{2},j+\frac{1}{2}}}{V_{i,j}}\right)\frac{A_{i-\frac{1}{2},j-\frac{1}{2}}}{A_{i,j}}\right]$$

First Order Temporal Distribution to Node i,j+1:

$$\Delta U_{i+\frac{1}{2},j+\frac{1}{2}}\left[\frac{1}{4}\left(\frac{V_{i+\frac{1}{2},j+\frac{1}{2}}}{V_{i,j+1}}\right)\frac{A_{i-\frac{1}{2},j+\frac{3}{2}}}{A_{i,j+1}}\right]$$

where the area terms, $A_{i,j}$, are defined as follows:

Equation 40: Two-Dimensional Area Terms (z-r plane)

$$A_{i-\frac{1}{2},j-\frac{1}{2}} = \frac{1}{2}\left(\begin{array}{l}\left(r_{i,j} - r_{i-1,j-1}\right)\left(z_{i,j-1} - z_{i-1,j}\right)+ \\ \left(r_{i-1,j} - r_{i,j-1}\right)\left(z_{i,j} - z_{i-1,j-1}\right)\end{array}\right)$$

$$A_{i-\frac{1}{2},j+\frac{3}{2}} = \frac{1}{2}\left(\begin{array}{l}\left(r_{i,j+2} - r_{i-1,j+1}\right)\left(z_{i,j+1} - z_{i-1,j+2}\right)+ \\ \left(r_{i-1,j+2} - r_{i,j+1}\right)\left(z_{i,j+2} - z_{i-1,j+1}\right)\end{array}\right)$$

$$A_{i+\frac{3}{2},j-\frac{1}{2}} = \frac{1}{2}\left(\begin{array}{l}\left(r_{i+2,j} - r_{i+1,j-1}\right)\left(z_{i+2,j-1} - z_{i+1,j}\right)+ \\ \left(r_{i+1,j} - r_{i+2,j-1}\right)\left(z_{i+2,j} - z_{i+1,j-1}\right)\end{array}\right)$$

$$A_{i+\frac{3}{2},j+\frac{3}{2}} = \frac{1}{2}\left(\begin{array}{l}\left(r_{i+2,j+2} - r_{i+1,j+1}\right)\left(z_{i+2,j+1} - z_{i+1,j+2}\right)+ \\ \left(r_{i+1,j+2} - r_{i+2,j+1}\right)\left(z_{i+2,j+2} - z_{i+1,j+1}\right)\end{array}\right)$$

The preceding simplification of the interpolation method presents two variations from the original Ni scheme[9]: 1) a simple area ratio to correct two-dimensional grid stretching and 2) a volume ratio that also corrects for grid stretching, but more importantly accounts for radial volume expansion in axisymmetric systems through an inherent radius ratio. More specifically, the area ratio weights the temporal changes closest to the node greater, thereby ensuring that the nodal changes are more influenced by the nearest cell-centered changes; as should be the case. The volume ratio weights the temporal changes greater when distributing from a cell with greater volume, which thereby accounts for the additional mass, momentum, and energy contained within that volume. In general, the distribution from large volume cells which lie nearest to a shared node will have greatest influence over the resulting nodal temporal changes because that distribution represents the bulk properties pertaining to the node. Again it is important to note that for a two-dimensional Cartesian system with a uniform grid, as considered by Ni[9], the above equations reduce to a one-quarter (homogeneous) distribution. In contrast, for an axisymmetric system with a uniform grid, the equations reduce to one-quarter the radius ratio (ratio of cell-center radius to distribution node radius) as shown below, which is the crucial extension of the original Ni scheme to cylindrical coordinates.

Axisymmetric Uniform Grid Distributions to Node i+1,j+1:

$$\Delta U_{i+\frac{1}{2},j+\frac{1}{2}} \frac{1}{4}\left(\frac{r_{i+\frac{1}{2},j+\frac{1}{2}}}{r_{i+1,j+1}}\right)$$

Axisymmetric Uniform Grid Distributions to Node i+1,j:

$$\Delta U_{i+\frac{1}{2},j+\frac{1}{2}} \frac{1}{4}\left(\frac{r_{i+\frac{1}{2},j+\frac{1}{2}}}{r_{i+1,j}}\right)$$

Axisymmetric Uniform Grid Distributions to Node i,j:

$$\Delta U_{i+\frac{1}{2},j+\frac{1}{2}} \frac{1}{4}\left(\frac{r_{i+\frac{1}{2},j+\frac{1}{2}}}{r_{i,j}}\right)$$

Axisymmetric Uniform Grid Distributions to Node i,j+1:

$$\Delta U_{i+\frac{1}{2},j+\frac{1}{2}} \frac{1}{4}\left(\frac{r_{i+\frac{1}{2},j+\frac{1}{2}}}{r_{i,j+1}}\right)$$

Though a subtle point, with a uniform grid, the reduction to one-quarter the radius ratio for an axisymmetric system is very important because distributions from greater radii should influence the nodal changes more than distribution from lower radii. As previously mentioned, this is because the volume is greater at larger radii and thus more mass, momentum, and energy is contained within the corresponding cells.

4.3 Calculation of Second Order Temporal Terms

Similar to the distribution of the first order temporal changes, the calculation of the second order temporal terms for an axisymmetric system require corrections for the radial volume expansion. As outlined in Section 3, Ni[9] decouples the offset integration of the second order temporal changes so that cell-based contributions to the nodal changes can be found inclusively within each cell and then distributed to the nodes along with the first order changes. This is obtained as a result of the first order differential characteristics of the Euler equations, where the second order temporal terms can be formulated as follows[9]:

Equation 41: Second Order Temporal Euler Terms

$$\frac{\Delta t^2}{2}\frac{\partial^2 U}{\partial t^2} = \frac{\Delta t}{2}\left[-\frac{\partial}{\partial z}\left[\underbrace{\left(\frac{\partial F}{\partial U}\right)\frac{\partial U}{\partial t}\Delta t}_{\Delta F}\right] - \frac{1}{r}\frac{\partial}{\partial r}\left[r\underbrace{\left(\frac{\partial G}{\partial U}\right)\frac{\partial U}{\partial t}\Delta t}_{\Delta G}\right]\right]$$

where $(\partial F/\partial U)$ and $(\partial G/\partial U)$ are the Jacobians of F and G, respectively. Referring to Ni[9] and the remarks of Section 3, the terms $(\partial F/\partial U)$ $(\partial U/\partial t)$ and $(\partial G/\partial U)$ $(\partial U/\partial t)$ are determined from the first order temporal terms and are thus known at the cell centers. Therefore, a control volume integration of Equation 41 around each node, along an offset grid and using the surrounding cell centered first order temporal terms, will resolve the second order temporal terms at each node. Referring to the layout shown in Figure 3, the integration is defined as

Equation 42: Integral of Second Order Temporal Terms (Euler Eqs.)

$$\int\left[\frac{\Delta t^2}{2}\frac{\partial^2 U}{\partial t^2}\right]dV_{i,j}=\frac{\Delta t}{2}\left[-\oint(\Delta F)rd\theta dr+\oint(\Delta G)rd\theta dz\right]$$

where ΔF and ΔG are defined in Equation 41.

Using finite volumes, the integration along the offset grid produces the following equation:

$$\left.\frac{\Delta t^2}{2}\frac{\partial^2 U}{\partial t^2}\right|_{i,j}=\frac{\Delta t}{2V_{i,j}}\left[\begin{array}{l}
\frac{1}{4}\left(\Delta F_{i-\frac{1}{2},j-\frac{1}{2}}+\Delta F_{i+\frac{1}{2},j-\frac{1}{2}}\right)\left(r_{i+\frac{1}{2},j-\frac{1}{2}}-r_{i-\frac{1}{2},j-\frac{1}{2}}\right)\left(r_{i+\frac{1}{2},j-\frac{1}{2}}+r_{i-\frac{1}{2},j-\frac{1}{2}}\right)+\\
\frac{1}{4}\left(\Delta F_{i+\frac{1}{2},j+\frac{1}{2}}+\Delta F_{i+\frac{1}{2},j-\frac{1}{2}}\right)\left(r_{i+\frac{1}{2},j+\frac{1}{2}}-r_{i+\frac{1}{2},j-\frac{1}{2}}\right)\left(r_{i+\frac{1}{2},j+\frac{1}{2}}+r_{i+\frac{1}{2},j-\frac{1}{2}}\right)-\\
\frac{1}{4}\left(\Delta F_{i-\frac{1}{2},j+\frac{1}{2}}+\Delta F_{i+\frac{1}{2},j+\frac{1}{2}}\right)\left(r_{i-\frac{1}{2},j+\frac{1}{2}}-r_{i+\frac{1}{2},j+\frac{1}{2}}\right)\left(r_{i-\frac{1}{2},j+\frac{1}{2}}+r_{i+\frac{1}{2},j+\frac{1}{2}}\right)-\\
\frac{1}{4}\left(\Delta F_{i-\frac{1}{2},j+\frac{1}{2}}+\Delta F_{i-\frac{1}{2},j-\frac{1}{2}}\right)\left(r_{i-\frac{1}{2},j+\frac{1}{2}}-r_{i-\frac{1}{2},j-\frac{1}{2}}\right)\left(r_{i-\frac{1}{2},j+\frac{1}{2}}+r_{i-\frac{1}{2},j-\frac{1}{2}}\right)-\\
\frac{1}{4}\left(\Delta G_{i-\frac{1}{2},j-\frac{1}{2}}+\Delta G_{i+\frac{1}{2},j-\frac{1}{2}}\right)\left(z_{i+\frac{1}{2},j-\frac{1}{2}}-z_{i-\frac{1}{2},j-\frac{1}{2}}\right)\left(r_{i+\frac{1}{2},j-\frac{1}{2}}+r_{i-\frac{1}{2},j-\frac{1}{2}}\right)-\\
\frac{1}{4}\left(\Delta G_{i+\frac{1}{2},j+\frac{1}{2}}+\Delta G_{i+\frac{1}{2},j-\frac{1}{2}}\right)\left(z_{i+\frac{1}{2},j+\frac{1}{2}}-z_{i+\frac{1}{2},j-\frac{1}{2}}\right)\left(r_{i+\frac{1}{2},j+\frac{1}{2}}+r_{i+\frac{1}{2},j-\frac{1}{2}}\right)+\\
\frac{1}{4}\left(\Delta G_{i-\frac{1}{2},j+\frac{1}{2}}+\Delta G_{i+\frac{1}{2},j+\frac{1}{2}}\right)\left(z_{i-\frac{1}{2},j+\frac{1}{2}}-z_{i+\frac{1}{2},j+\frac{1}{2}}\right)\left(r_{i-\frac{1}{2},j+\frac{1}{2}}+r_{i+\frac{1}{2},j+\frac{1}{2}}\right)+\\
\frac{1}{4}\left(\Delta G_{i-\frac{1}{2},j+\frac{1}{2}}+\Delta G_{i-\frac{1}{2},j-\frac{1}{2}}\right)\left(z_{i-\frac{1}{2},j+\frac{1}{2}}-z_{i-\frac{1}{2},j-\frac{1}{2}}\right)\left(r_{i-\frac{1}{2},j+\frac{1}{2}}+r_{i-\frac{1}{2},j-\frac{1}{2}}\right)
\end{array}\right]$$

Decoupling this equation into piecewise distributions of second order temporal term contributions, similar to the first order term interpolation method, the control volume integration becomes cell based, thereby allowing cell contributions to be determined autonomously and agglomerated at the respective nodes; as was done by Ni[9] for two-dimensional Cartesian systems. After expansion and simplification (shown in Appendix A) of the above equation, the area terms $rd\theta dr$ and $rd\theta dz$ can be approximated to cell-based areas by referring to Figures 2 and 4. Relating back to the original Ni scheme, for a two-dimensional Cartesian system with a uniform grid approximation, the above equation would reduce to the second order distribution formulas given by Ni[9]. For an axisymmetric system though, with radial volume expansion considerations, the second order temporal distributions to each node simplify to:

Second Order Temporal Distribution to Node i+1,j+1:

$$\frac{\Delta t}{4V_{i+1,j+1}}\left[\begin{array}{l}
\Delta F dA r_{EW}\left(\frac{r_{i+1,j+\frac{1}{2}}}{r_{i+\frac{1}{2},j+\frac{1}{2}}}\right)-\Delta F dA r_{NS}\left(\frac{r_{i+\frac{1}{2},j+1}}{r_{i+\frac{1}{2},j+\frac{1}{2}}}\right)\\
-\Delta G dA z_{EW}\left(\frac{r_{i+1,j+\frac{1}{2}}}{r_{i+\frac{1}{2},j+\frac{1}{2}}}\right)+\Delta G dA z_{NS}\left(\frac{r_{i+\frac{1}{2},j+1}}{r_{i+\frac{1}{2},j+\frac{1}{2}}}\right)
\end{array}\right]$$

Second Order Temporal Distribution to Node i+1,j:

$$\frac{\Delta t}{4V_{i+1,j}}\left[\begin{array}{l}-\Delta FdAr_{EW}\left(\dfrac{r_{i+1,j+\frac{1}{2}}}{r_{i+\frac{1}{2},j+\frac{1}{2}}}\right)-\Delta FdAr_{NS}\left(\dfrac{r_{i,j+\frac{1}{2}}}{r_{i+\frac{1}{2},j+\frac{1}{2}}}\right)\\+\Delta GdAz_{EW}\left(\dfrac{r_{i+1,j+\frac{1}{2}}}{r_{i+\frac{1}{2},j+\frac{1}{2}}}\right)+\Delta GdAz_{NS}\left(\dfrac{r_{i,j+\frac{1}{2}}}{r_{i+\frac{1}{2},j+\frac{1}{2}}}\right)\end{array}\right]$$

Second Order Temporal Distribution to Node i,j:

$$\frac{\Delta t}{4V_{i,j}}\left[\begin{array}{l}-\Delta FdAr_{EW}\left(\dfrac{r_{i,j+\frac{1}{2}}}{r_{i+\frac{1}{2},j+\frac{1}{2}}}\right)+\Delta FdAr_{NS}\left(\dfrac{r_{i+\frac{1}{2},j}}{r_{i+\frac{1}{2},j+\frac{1}{2}}}\right)\\+\Delta GdAz_{EW}\left(\dfrac{r_{i,j+\frac{1}{2}}}{r_{i+\frac{1}{2},j+\frac{1}{2}}}\right)-\Delta GdAz_{NS}\left(\dfrac{r_{i+\frac{1}{2},j}}{r_{i+\frac{1}{2},j+\frac{1}{2}}}\right)\end{array}\right]$$

Second Order Temporal Distribution to Node i,j+1:

$$\frac{\Delta t}{4V_{i,j+1}}\left[\begin{array}{l}\Delta FdAr_{EW}\left(\dfrac{r_{i,j+\frac{1}{2}}}{r_{i+\frac{1}{2},j+\frac{1}{2}}}\right)+\Delta FdAr_{NS}\left(\dfrac{r_{i+\frac{1}{2},j+1}}{r_{i+\frac{1}{2},j+\frac{1}{2}}}\right)\\-\Delta GdAz_{EW}\left(\dfrac{r_{i,j+\frac{1}{2}}}{r_{i+\frac{1}{2},j+\frac{1}{2}}}\right)-\Delta GdAz_{NS}\left(\dfrac{r_{i+\frac{1}{2},j+1}}{r_{i+\frac{1}{2},j+\frac{1}{2}}}\right)\end{array}\right]$$

Again, the extension to cylindrical coordinates introduces a radius ratio term to account for radial volume expansion. More specifically, the radius ratios correct the $rd\theta$ terms in the piecewise finite-volume integration to be more representative of true integration around the nodes, which requires an offset grid and the coupling of cell contributions.

4.4 General Two-Dimensional Axisymmetric Distribution Formulas

Here, the first and second order temporal terms are combined in a form similar to that presented by Ni[9] for comparison. Referring again to the layout shown in Figure 4 and the piecewise contributions to a single node, the general second order two-dimensional axisymmetric solution of the Euler equations through a piecewise distribution method is:

$$\Delta f = \frac{\Delta t}{V_{i,j}}\left(\Delta F\, dAr_{NS} - \Delta G\, dAz_{NS}\right)$$

$$\Delta g = \frac{\Delta t}{V_{i,j}}\left(\Delta F\, dAr_{EW} - \Delta G\, dAz_{EW}\right)$$

$$\delta U_{i+\frac{1}{2},j+\frac{1}{2}} = \frac{1}{4}\left[\Delta U_{i+\frac{1}{2},j+\frac{1}{2}}\left(\frac{V_{i+\frac{1}{2},j+\frac{1}{2}}}{V_{i+1,j+1}}\right)\left(\frac{A_{i+\frac{3}{2},j+\frac{3}{2}}}{A_{i+1,j+1}}\right) - \Delta f_{i+\frac{1}{2},j+\frac{1}{2}}\left(\frac{r_{i+\frac{1}{2},j+1}}{r_{i+\frac{1}{2},j+\frac{1}{2}}}\right) + \Delta g_{i+\frac{1}{2},j+\frac{1}{2}}\left(\frac{r_{i+1,j+\frac{1}{2}}}{r_{i+\frac{1}{2},j+\frac{1}{2}}}\right)\right]$$

$$\delta U_{i+1,j} = \frac{1}{4}\left[\Delta U_{i+\frac{1}{2},j+\frac{1}{2}}\left(\frac{V_{i+\frac{1}{2},j+\frac{1}{2}}}{V_{i+1,j}}\right)\left(\frac{A_{i+\frac{3}{2},j-\frac{1}{2}}}{A_{i+1,j}}\right) - \Delta f_{i+\frac{1}{2},j+\frac{1}{2}}\left(\frac{r_{i+\frac{1}{2},j}}{r_{i+\frac{1}{2},j+\frac{1}{2}}}\right) - \Delta g_{i+\frac{1}{2},j+\frac{1}{2}}\left(\frac{r_{i+1,j+\frac{1}{2}}}{r_{i+\frac{1}{2},j+\frac{1}{2}}}\right)\right]$$

$$\delta U_{i,j} = \frac{1}{4}\left[\Delta U_{i+\frac{1}{2},j+\frac{1}{2}}\left(\frac{V_{i+\frac{1}{2},j+\frac{1}{2}}}{V_{i,j}}\right)\left(\frac{A_{i-\frac{1}{2},j-\frac{1}{2}}}{A_{i,j}}\right) + \Delta f_{i+\frac{1}{2},j+\frac{1}{2}}\left(\frac{r_{i+\frac{1}{2},j}}{r_{i+\frac{1}{2},j+\frac{1}{2}}}\right) - \Delta g_{i+\frac{1}{2},j+\frac{1}{2}}\left(\frac{r_{i,j+\frac{1}{2}}}{r_{i+\frac{1}{2},j+\frac{1}{2}}}\right)\right]$$

$$\delta U_{i,j+1} = \frac{1}{4}\left[\Delta U_{i+\frac{1}{2},j+\frac{1}{2}}\left(\frac{V_{i+\frac{1}{2},j+\frac{1}{2}}}{V_{i,j+1}}\right)\left(\frac{A_{i-\frac{1}{2},j+\frac{3}{2}}}{A_{i,j+1}}\right) + \Delta f_{i+\frac{1}{2},j+\frac{1}{2}}\left(\frac{r_{i+\frac{1}{2},j+1}}{r_{i+\frac{1}{2},j+\frac{1}{2}}}\right) + \Delta g_{i+\frac{1}{2},j+\frac{1}{2}}\left(\frac{r_{i,j+\frac{1}{2}}}{r_{i+\frac{1}{2},j+\frac{1}{2}}}\right)\right]$$

5 Additional Numerical Techniques

5.1 Data Structure

A multi-block, point-matched, structured-grid strategy is currently used where blocks are constructed from multiple faces. Each face of a block is allowed to have an arbitrary number of sub-faces to enable virtually any connectivity of blocks and any combination of boundary conditions along a face of a block. Blocks may have any arbitrary orientation relative to the adjoining blocks. Block connectivity and boundary condition information is defined by a global connectivity file that stores global block number, block rotational speed, and information for each sub-face of each face. The sub-face information includes the physical boundary condition type or the adjoining block number, the starting and ending indices of the sub-face, the starting and ending indices of the adjoining sub-face, and any auxiliary physical boundary condition information. The block connectivity file is either constructed by the user or automatically produced by a grid generation procedure.

5.2 Control of Numerical Dissipation

A new approach to numerical dissipation is introduced. In central-difference codes, artificial dissipation is used to control odd-even decoupling and to capture shocks. The combined second- and fourth-difference dissipation model of Jameson[13] is used in the current procedures for both the mean flow and turbulence transport equations. It is a common practice to decay, or scale, the numerical dissipation through the viscous flow regions so that the numerical dissipation does not overwhelm the conservation equation fluxes. Various approaches have been used previously to perform this function. Jameson[13] suggests scaling the dissipation fluxes by the time-step multiplied by the spectral radius. This scaling essentially decays the numerical smoothing based on the local minimum grid spacing. Thus, in regions of fine-grid spacing such as in the boundary layer regions, the numerical dissipation is decreased. The disadvantage to this approach is that viscous flow regions, including wakes or large eddy structures, often occur in regions where the computational grid is not clustered. As a result, the structure and physical effects of these viscous flows can be damped. Chima[14] decayed numerical dissipation through the viscous flow regions

using a Mach number function. The disadvantage of using either a velocity or Mach number function is that inviscid regions of low-speed or low Mach number flow can often exist in the domain. As a result, the numerical dissipation can be decayed in regions where it should not. Davis et al.[11,12] decayed the numerical dissipation through boundary layers by determining the boundary layer length scales and then decaying the numerical dissipation using exponential functions. This approach works well for boundary layer flows, but unfortunately does not address the need to decay the numerical dissipation in general viscous flow regions.

In the current procedure, the fourth-difference dissipation is scaled by the inverse of the absolute value of the strain rate magnitude squared. This function decays the numerical dissipation in all viscous flow regions, including boundary layers, wakes, large eddies, secondary flows, etc.

With the decay of numerical smoothing being of particular interest within boundary layers and regions of large velocity gradients, scaling proportional to strain rate, which is generated by velocity gradients, is ideal. Of the strain rate components, the off-diagonal terms within the strain rate tensor that are proportional to normal velocity gradients, which define boundary layers, wakes, eddies, and secondary flow regions, are of particular interest and are define as:

Equation 43: Axisymmetric Off-Diagonal Strain Rate Components

$$S_{ij} = \frac{1}{2}\partial_i v_j + \frac{1}{2}\partial_j v_i$$

$$S_{\theta r} = S_{r\theta} = \frac{1}{2}\left[r\frac{\partial}{\partial r}\left(\frac{w}{r}\right)\right]$$

$$S_{z\theta} = S_{\theta z} = \frac{1}{2}\left[\frac{\partial w}{\partial z}\right]$$

$$S_{rz} = S_{zr} = \frac{1}{2}\left[\frac{\partial v}{\partial z} + \frac{\partial u}{\partial r}\right]$$

5.3 Decomposition, Parallelization, and Agglomeration

Decomposition of the computational domain is performed in a separate grid generation procedure. This procedure generates a smooth, stretched computational grid using an algebraically generated initial grid that is smoothed with a multi-block Poisson technique[15,16]. Decomposition of the initial multi-block grid into additional grid blocks to enhance parallelization of the solution is performed using an optimization procedure that attempts to load balance the

resulting blocks as much as possible. The grid generation procedure produces a computational grid file as well as the global connectivity file that describes block neighbor and boundary condition information.

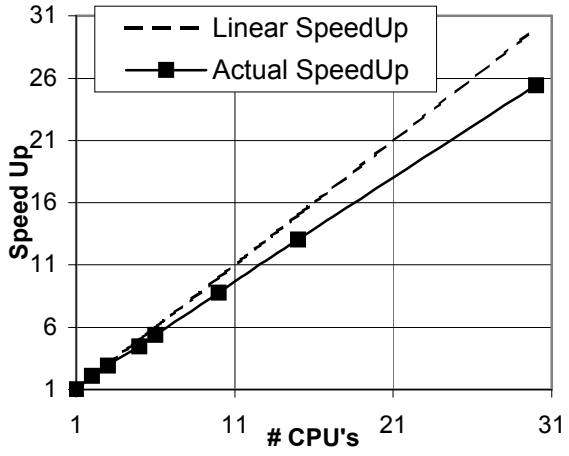

Figure 5: Processor speed up as Function of Number of Processors

Parallelization is performed using the Message Passing Interface (MPI) library[17]. Message passing is limited to a single subroutine for each of the flow and turbulence solvers to reduce overhead and allow for scalable parallelization. In these routines, non-blocking, immediate send and receive messages are used to efficiently pass information between processors. Figure 5 shows the typical speed-up as a function of the number of processors. The configuration used to generate this data was a turbine cascade of 34,000 grid points and 30 blocks. This data was generated on a Linux cluster consisting of 2.6GHz Athalon cpus. Figure 5 shows that a speed-up factor of 25.5 is realized with 30 processors yielding an 85% parallel efficiency, which is considered good for a two-dimensional procedure with this number of grid points. As a result, the computational turn-around time per grid point, per iteration using 30 processors is 2×10^{-6} secs. Typical time-averaged, detached-eddy simulations of configurations with a similar grid density in which a steady RANS solution followed by an unsteady detached-eddy solution and time-averaging over an appropriate period can be performed in less than 1 hour clock time.

It can be tedious to post-process solutions in which the computational domain has been decomposed into many blocks. Creating continuous pressure distributions or integrating quantities requires knowledge of the block connectivity. Post-processing could be done entirely

within the flow solution procedure that stores this information. However, it is desirable to also be able to post-process information in a separate procedure. To simplify this separate post-processing step, the decomposed set of blocks is agglomerated to a minimal number of blocks. This ability greatly expedites the post-processing of pressure distributions, boundary layer characteristics, and aerodynamic performance quantities.

5.4 Automation

Several automation techniques have been added in order to produce time-averaged detached-eddy simulation results in the same turn-around time as traditional "steady" Reynolds-averaged Navier-Stokes simulations. For instance, a detached-eddy simulation consists of the following automated steps to provide solution acceleration and the engineering information relevant to design:

1. read global aerodynamic, connectivity, and computational grid information
2. define initial conditions of all flow variables
3. perform decomposition of blocks to processors via processor restart files
4. each processor reads its own restart files consisting of individual connectivity, grid, and initial flow files
5. perform a steady, Reynolds-averaged Navier-Stokes solution (used for comparison with the detached-eddy solution)
6. write a global, steady, RANS solution file that is agglomerated back to a minimal number of blocks defined by the user to simplify post-processing
7. continue with a time-accurate detached-eddy simulation for a specified number of time-steps
8. over a prescribed time interval, time-average the detached-eddy simulation and write a global, agglomerated instantaneous restart file for post-processing and solution animation
9. write out the global time-averaged, agglomerated detached-eddy simulation results

6 Axisymmetric Numerical Instability for Strong Rotation

Several numerical instabilities exist for axisymmetric flows with strong rotation and though general numerical techniques for stability will not be presented, the issues are addressed and several approaches of common practice are outlined. Of greatest importance are the source-terms inherent in the cylindrical Navier-Stokes equations. Referring to Eqs. 10 and 11, the following terms:

Equation 44: Axisymmetric Source Terms

$$\int \frac{\partial \rho v}{\partial t} dV_{ol} = \ldots + \int \frac{\left(p + \rho w^2\right)}{r} dV_{ol}$$

$$\int \frac{\partial \rho w}{\partial t} dV_{ol} = \ldots - \int \frac{\rho v w}{r} dV_{ol}$$

cause the differential nature of the N-S equations to become extremely stiff under strong rotation, thereby severely slowing convergence and requiring sufficiently accurate initial conditions. Without accurately initializing to near steady-state flow conditions for strong rotation systems, these terms can quickly become divergent sources through coupled growth, and a reasonable reduction in CFL number may not assist convergence. To avoid the instabilities resulting from the source terms, common practice often requires a transient increase in rotational speeds or the generation of a library of steady state rotational flow solutions, which allows incremental solutions at increasing rotational rates. Both methods require RANS solutions at several rotational rates when analyzing flows with strong rotation, which is computationally inefficient but often accepted.

In addition to the source terms, large scale decoupling between the momentum equations can occur when analyzing purely rotational flows; as seen in gaseous diffusion systems. In this case, as the rotational rate increases the transient effect of the source terms and round-off accumulation or error grouping (defined as the grouping of similar small changes in particular regions of the domain) can cause decoupling of the momentum equations. This can particularly happen with the axial momentum equation because of the negligible velocity contribution and insignificant viscous dissipation, both of which assist the inclination to decouple. An example of the large scale decoupling caused by the interaction of rotational source terms and round-off accumulation (error-grouping) is shown in Figure 6:

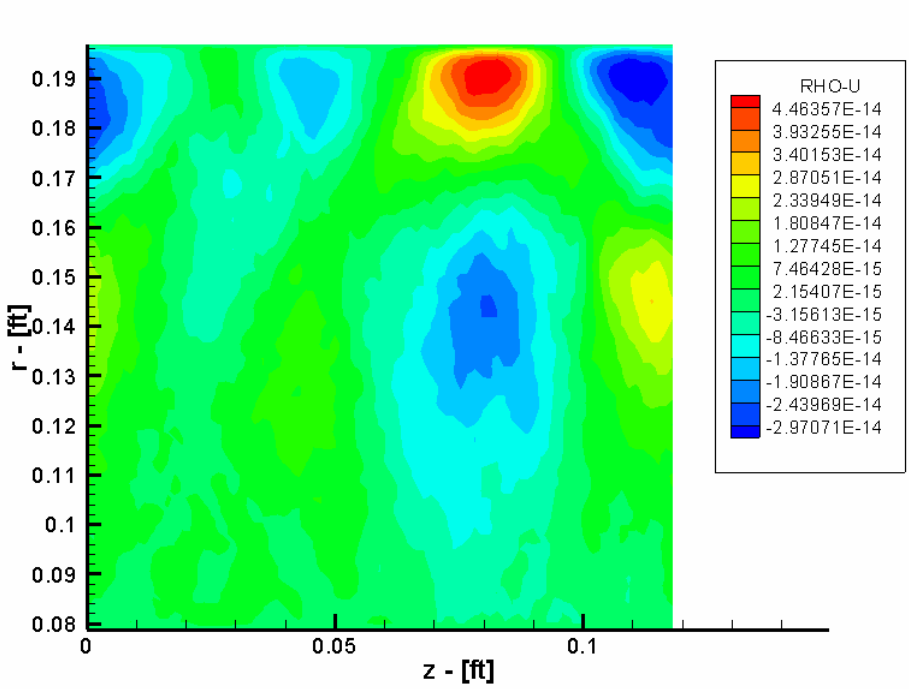

Figure 6: Axial Momentum (ρu) Large Scale Decoupling

To avoid the decoupling effect, limited equation convergence has been attempted. More specifically, excluding one momentum equation may allow steady state solution, where upon convergence the rotational source terms reduce in magnitude and instability. With the limited equation converged solution, iteration on the full set of equations may be possible without decoupling, thereby providing an accurate solution. The exclusion of certain equations, or even certain terms, is a means to generate a more sufficient initial condition, one which avoids numerical instabilities.

7 Boundary Conditions

In most cases, the stagnation pressure, stagnation temperature, and flow angle are held to specified quantities at the inlet to the domain. Then at the exit of the domain, the static pressure is usually held to a specified value in order to establish the desired pressure gradient, which thereby allows the prediction of the flow variables. In some special situations, such as when multiple inlet and exit boundaries exist, it can be more definitive to hold the mass-flow rate at the inlets and/or exits.

The majority of rotating flows correspond to internal flow conditions where accurate experimental flow data is sparse. In the most complicated systems, it is often still possible to obtain accurate mass flow, stagnation temperature, and stagnation or static pressure measurements at the systems boundaries and thus numerical domain boundaries are often treated using specified mass flow conditions.

Solid walls may be modeled as either slip or no-slip conditions. Walls in which the viscous layers are extremely thin or where the viscous effects are of no concern may be modeled using the slip condition with which the flow is kept tangent to the surface. For walls that have adjacent viscous layers considered to be important, the no-slip condition is used where the velocity of the fluid takes on the velocity of the wall at the surface. In addition, the flow at the wall may be considered to be adiabatic (no heat transfer to/from the wall) or have a specified temperature or heat-flux along the wall.

7.1 Inlet Boundary Conditions

At the inlet to internal flow systems, the stagnation temperature and absolute flow angle are held fixed to specified values that correspond to experimental data and inlet geometry, respectively. In most cases, the inlet flow angle is normal to the surface but for applications such as film cooling, the inlet geometry may be severely angled to allow the inlet flow to disperse within the boundary layer rather than into the main flow.

7.1.1 Non-Iterative Prescribed Mass-Flow Method

In addition to stagnation temperature and absolute flow angle, either the stagnation pressure or mass flow rate may be prescribed. If stagnation pressure is held, then the total mass flow rate and its distribution throughout the system are predicted[18]. Analysis by Davis et al.[18] discovered that setting the stagnation pressure alone could result in negative flow at system boundaries due to large pressure transients incurred during convergence. It was found that mass flow rate should be held constant along inlets to be consistent with available data. Additionally, setting the mass flow rate provides control over the total flow rate going into the system and thus allows the inlet flow rate to be set to experimental data or design intent[18].

With the mass flux, computed from the specified mass flow $\dot{m}$ and inlet area A_{in}, the inlet density may be calculated from the enthalpy relationship and equation of state as follows:

Equation 45: Inlet Density Derivation for Mass Flow Boundary Conditions

$$h_t = h_s + \frac{1}{2}V^2$$

$$\textit{where} \quad h_s = c_p T_s$$

$$h_t = c_p T_t$$

$$\dot{m} = \rho A V$$

$$P_s = \rho R T_s$$

$$\textit{thus},$$

$$c_p T_t = c_p T_s + \frac{1}{2\rho^2}\left(\frac{\dot{m}}{A}\right)^2$$

$$\rho^2 T_t = \frac{\rho P_s}{R} + \frac{1}{2c_p}\left(\frac{\dot{m}}{A}\right)^2$$

$$\textit{or} \qquad \rho^2 T_t - \frac{\rho P_s}{R} - \frac{1}{2c_p}\left(\frac{\dot{m}}{A}\right)^2 = 0$$

The inlet density may be found by solving the above quadratic equation:

Equation 46: Inlet Density for Mass Flow Boundary Conditions

$$\rho_{new} = \left[\frac{P_s}{R} + \sqrt{\left(\frac{P_s}{R}\right)^2 + \frac{2T_t\left(\frac{\dot{m}}{A}\right)^2}{c_p}}\right] \Big/ 2T_t$$

where the static pressure (P_s) is taken from one node inside of the domain, normal to the inlet boundary. Once the inlet density is determined from Equation 46, the velocity components are calculated from the mass flux ($\dot{m}/A$) and the prescribed inlet flow angles. As shown by Davis et al.[18], the boundary condition described is equivalent to extrapolating the static temperature and

iterating on total pressure until obtaining the desired flow rate. The remainder of the inlet flow variables can be found as shown:

Equation 47: Inlet Flow Variables

$$V_{new} = \left(\frac{\dot{m}}{A}\right)\frac{1}{\rho_{new}}$$

$$T_s = T_t - \frac{1}{2c_p}V_{new}^2$$

$$P_{t\,new} = P_s\left(\frac{T_t}{T_s}\right)^{\frac{\gamma}{(\gamma-1)}}$$

$$E = \frac{P_s}{\gamma - 1} + \frac{1}{2}\rho_{new}V_{new}^2$$

7.1.2 Iterative Prescribed Mass-Flow Method

In contrast to the previous method, prescribing both the stagnation pressure and mass flow rate allows the static pressure to be calculated from a predicted velocity, rather than vice versa. The total-mass flow parameter, $TMFP$, along with fixed total temperature, stagnation pressure, and mass flux ($\dot{m}/A$) are used to iteratively solve for the inlet Mach number as shown below:

Equation 48: Inlet Density for Mass Flow Boundary Conditions

$$TMFP(M) = \left(\frac{\dot{m}}{A}\right)\frac{\sqrt{T_T R/\gamma}}{P_T} = M\left(1 + \frac{\gamma-1}{2}M^2\right)^{\frac{-(\gamma+1)}{2(\gamma-1)}}$$

or

$$M = \frac{\dot{m}}{A}\sqrt{\frac{T_T R}{\gamma}}\frac{1}{P_T}\left(1 + \frac{\gamma-1}{2}M^2\right)^{\frac{\gamma+1}{2(\gamma-1)}}$$

The solution of Mach number only requires a couple iterations with an initial guess for Mach number of zero on the right-hand side and allowing the equation to iteratively converge. From Equation 48, the initial iteration can thus be formulated as:

Equation 49: Initial Mach Iteration

$$M_{init} = \frac{\dot{m}}{A}\sqrt{\frac{T_T R}{\gamma}}\frac{1}{P_T}$$

With the Mach number, the predicted inlet velocities set the static properties as shown:

Equation 50: Inlet Static Properties

$$T_s = \frac{V_{pred}^{\ 2}}{M^2 \gamma R}$$

$$h_t = c_p T_s - \frac{1}{2} V_{pred}^2$$

$$P_s = P_t \left(1 + \frac{\gamma - 1}{2} M^2 \right)^{-\gamma/\gamma - 1}$$

$$e = \rho h_t - P_s$$

where total enthalpy is also held constant.

7.2 Exit Boundary Conditions

There are two possible exit boundary conditions, the specification of a constant exit static pressure or mass flow rate. By holding the static pressure, the flow rate and flow splits, if there are multiple exits, are predicted. Conversely, setting the mass flow rate allows the exit pressure to be predicted through calculation of the exit Mach number, M_{exit}, from the total mass flow parameter using an iterative solution procedure, similar to the previous equations, as shown below:

Equation 51: Total Mass Flow Parameter (*TMFP*)

$$TMFP(M) = \left(\frac{\dot{m}}{A} \right)_{pres} \frac{\sqrt{T_{T\,exit} R/\gamma}}{P_{T\,exit}} = M_{exit} \left(1 + \frac{\gamma - 1}{2} M_{exit}^{\ 2} \right)^{\frac{-(\gamma+1)}{2(\gamma-1)}}$$

or

$$M_{exit} = \left(\frac{\dot{m}}{A} \right)_{pres} \sqrt{\frac{T_{T\,exit} R}{\gamma}} \frac{1}{P_{T\,exit}} \left(1 + \frac{\gamma - 1}{2} M_{exit}^{\ 2} \right)^{\frac{\gamma+1}{2(\gamma-1)}}$$

where $\dot{m}/A$ is the prescribed mass flux, P_{texit} is the predicted stagnation pressure, and T_{texit} is the predicted stagnation temperature. Again, two or three iterations are required to determine the exit Mach number using the initial guess described in Equation 49. With the exit Mach number, the exit static pressure required to deliver the prescribed mass flow rate may be found from the isentropic total-to-static pressure relationship and the local stagnation pressure[18], shown below:

Equation 52: Exit Static Properties

$$P_s = P_{t\,pred}\left(1+\frac{\gamma-1}{2}M_{exit}{}^2\right)^{-\gamma/\gamma-1}$$

$$T_s = \frac{V_{pred}{}^2}{M_{exit}{}^2\gamma R}$$

$$\rho = \frac{P_s}{RT_s}$$

$$h_s = c_p T_s$$

$$E = \frac{P_s}{\gamma-1}+\frac{1}{2}\rho V_{pred}{}^2$$

8 Results

Verification has been accomplished through several standard test cases such as laminar and turbulent flow through a pipe and concentric cylinders. Additionally, experimental case study validations, such as transonic flow over an axisymmetric bump, have supplemented analytical verification, particularly in the realm of turbulent flows. The results are shown in the following sub-sections to demonstrate accuracy and computational efficiency.

8.1 Laminar Pipe Flow

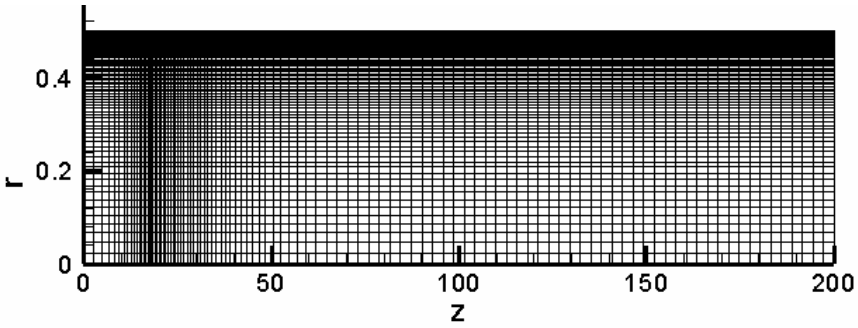

Figure 7: Computational grid for laminar pipe flow validation case

Analysis of laminar flow through a pipe at a Reynolds number, based on diameter, of 1800 was performed. The computational domain, shown in Figure 7, is constructed with 105 axial and 73 radial points. Hyperbolic stretching in both the axial and radial directions resolves the inlet and viscous wall boundary layers, respectively. The tangential spacing between the pipe wall and the first normal point is 9.144×10^{-2} m (3.0×10^{-3} ft). and when non-dimensionalized by the pipe diameter is 6×10^{-2}. Streamwise grid refinement produces a grid spacing of 0.1524 m (0.5 ft) at the leading edge of the pipe wall, which non-dimensionalized by the pipe length is 2.5×10^{-3}. The upstream boundary is placed 5.486 m (18 ft), equivalent to 18 pipe diameters (D), preceding the pipe inlet to ensure no upstream boundary interaction with the inlet. Similarly, to ensure fully developed flow, the laminar entrance length predicted from $L_e / d \approx 0.06 Re_d$ is 32.9m (108 ft) and therefore the pipe is modeled with a length of ~56.08m (184 ft). The pipe walls are modeled as no-slip, adiabatic and the centerline was modeled with a slip tangency boundary condition, in which radial fluxes are set to zero. Additionally, the inlet total pressure and the exit static

pressure are held at ~20.15 N/m^2 (.424 lbs/ft^2) and ~20.15 N/m^2 (.421 lbs/ft^2), respectively. The Mach number of the flow approaching the pipe is 0.1, which closely approximates incompressible flow as required by the analytical assumptions.

For verification with a fully developed laminar axisymmetric flow assumption, the resultant analytical equation for the axial velocity distribution, derived from a simplification of the N-S equations, is:

Equation 53: Axial Velocity Distribution for Laminar Pipe Flow

$$u(r) = \left(-\frac{\partial p}{\partial x}\right)\frac{R^2}{4\mu}\left(1-\frac{r^2}{R^2}\right)$$

where R is the pipe radius, r is the radial position, and $\partial p/\partial x$ is the axial pressure gradient.

The plot of axial velocity distribution in Figure 8 shows the numerically predicted velocity profile to be in effect, equivalent to the analytically determined velocity profile, which is evaluated with respect to the same pressure gradient. The maximum deviation between the numerical and analytical velocity profiles occurs along the pipe centerline and was <0.10%.

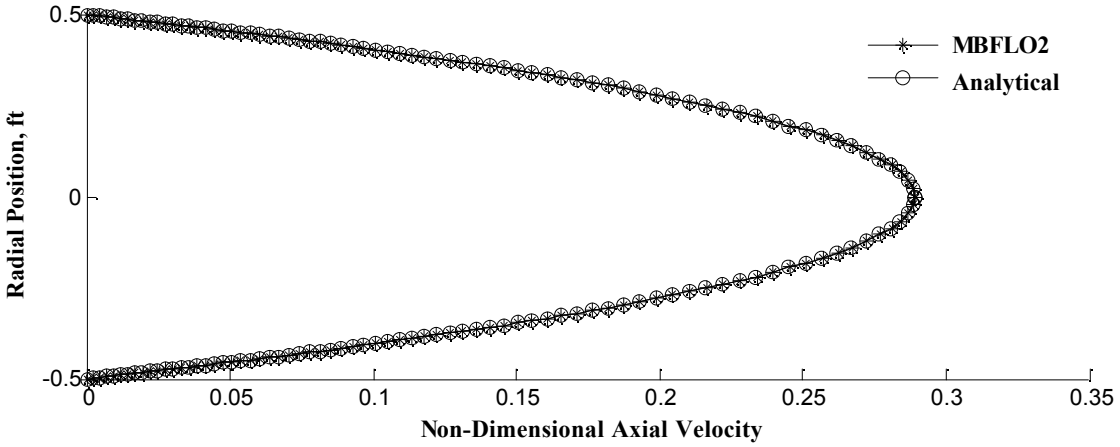

Figure 8: Numerical and Analytical axial velocity distributions for laminar pipe flow at Re_d=1800 and R=0.15m (0.5ft).

Figure 9 shows contours of the axial velocity (u) that portrays the flow funneling into the pipe, which corresponds to an upstream pressure chamber driving the fluid motion. The vertical contour lines at the inlet of the pipe represent the velocity gradient experienced during the transition from the free-stream, inviscid flow, to fully developed, pure viscous flow. Being laminar flow and low speed (Ma << .3), a velocity gradient only exists in the “entrance region” a short

length downstream of the inlet. Downstream of this “entrance length”, the straight axial contour lines represent steady fully developed flow where the velocity profile remains unchanged.

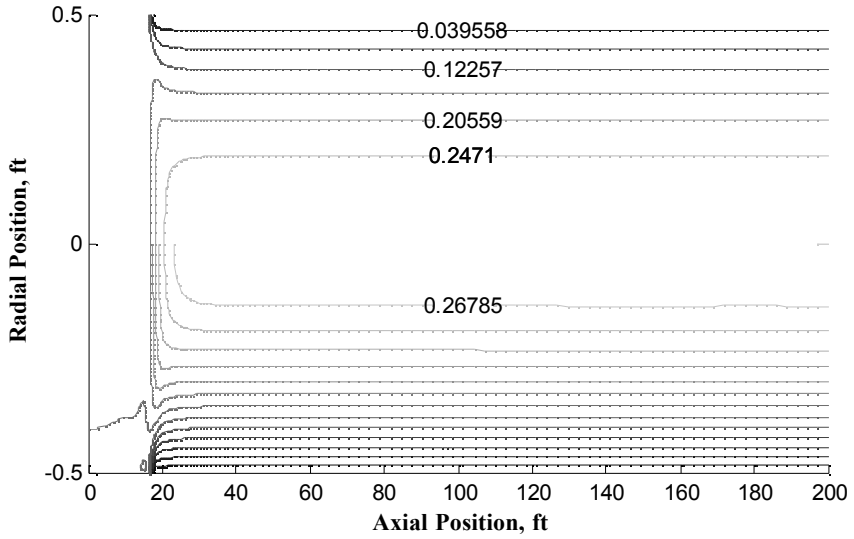

Figure 9: MBFLO2 axial velocity contours for laminar pipe flow at Red=1800 and R=0.15m (0.5ft).

8.2 Turbulent Pipe Flow

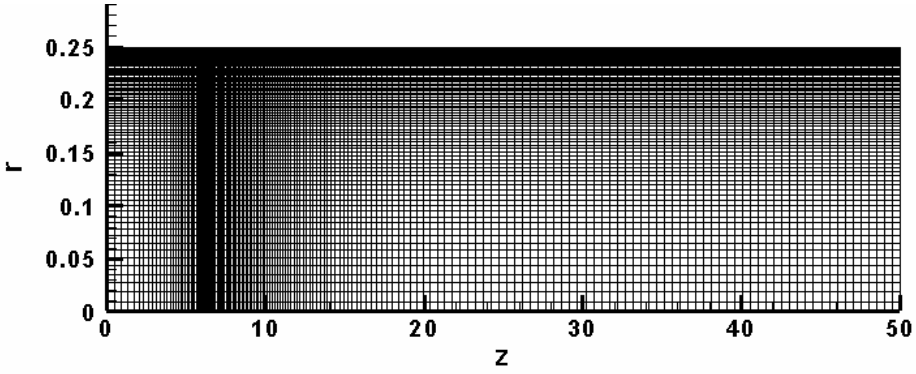

Figure 10: Computational grid for turbulent pipe flow validation case

Increasing the Reynolds number to 5 x 10^4, based on diameter, analysis of turbulent flow through a pipe was performed. The computational domain, shown in Figure 10, is constricted radially in comparison the laminar grid and comprised of 168 axial and 81 radial points. The increased grid density, compared to the laminar case, improves the resolution of both the near wall viscous layer and the outer turbulent layer. As was for the laminar case, hyperbolic stretching is used to resolve the inlet and viscous wall boundary layers. The tangential spacing between the pipe wall and the first normal point is 3.048 x 10^{-2} m (1 x 10^{-3} ft) and when non-

dimensionalized by the pipe diameter is 2 x 10^{-3}. Streamwise grid spacing at the leading edge of the pipe wall is < 3.048 x 10^{-2} m (0.1 ft), which non-dimensionalized by the pipe length is ~2.3 x 10^{-3}. The upstream boundary is placed 2.438 m (8 ft), equivalent to 16 pipe diameters (D), preceding the pipe inlet to prevent the boundaries influence on the main flow. The turbulent entrance length predicted from $L_e / d \approx 4.4 Re_d^{1/6}$ is 4.069 m (13.35 ft) and therefore the pipe is modeled with a length of ~13.106 m (43 ft) to ensure fully developed flow. The pipe walls are modeled as adiabatic with no-slip and the centerline is represented again with a slip tangency boundary condition. The inlet total pressure and the exit static pressure are held at ~63105.62 N/m^2 (1327.88 lbs/ft^2) and ~59285.67 N/m^2 (1247.50 lbs/ft^2), respectively. The Mach number of the flow approaching the pipe is 0.3.

For verification with a fully developed turbulent axisymmetric flow assumption, the following logarithmic law equation provides an analytical equation for the axial velocity distribution that nearly approximates experimental velocity profiles:

Equation 54: Axial Velocity Distribution for Turbulent Pipe Flow

$$u(r) \approx \frac{u^*}{0.41} \ln\left(\frac{(R-r)u^*}{v}\right) + 5.0$$

where R is the radial position of the pipe centerline (normally 0.0), r is the radial position in relation to the pipe wall, v is the kinematic viscosity, and u^* is the friction velocity defined by the law of the wall given below:

Equation 55: Law of the Wall

$$u^* = \left(\frac{\tau_w}{\rho}\right)^{1/2}$$

where τ_w is the wall shear stress and ρ is the density.

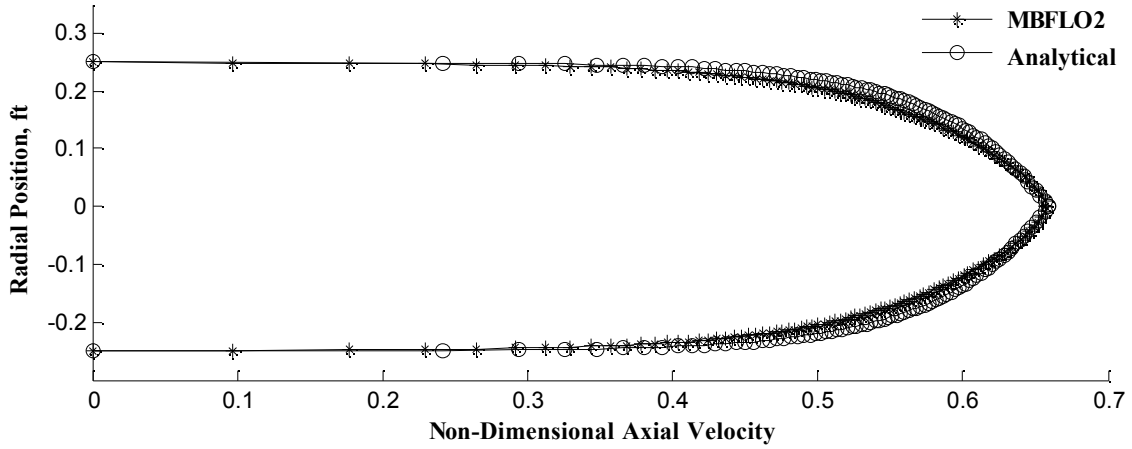

Figure 11: Numerical and Analytical axial velocity distributions for turbulent pipe flow at Re_d=50,000 and R=0.15m (0.5ft).

As was for the laminar case, the numerically predicted axial velocity distribution for turbulent pipe flow, shown in Figure 11, is consistent with the analytical log-law profile determined from the law of the wall. The slight disparity between the numerical and analytical velocity distributions is due to a greater shear stress associated with the log-law profile in the region between the inner viscous region and the overlap region (intermediate region where both laminar and turbulent shear are important), which is expected and experimentally outlined by White[19].

8.3 Laminar Flow through Concentric Cylinders

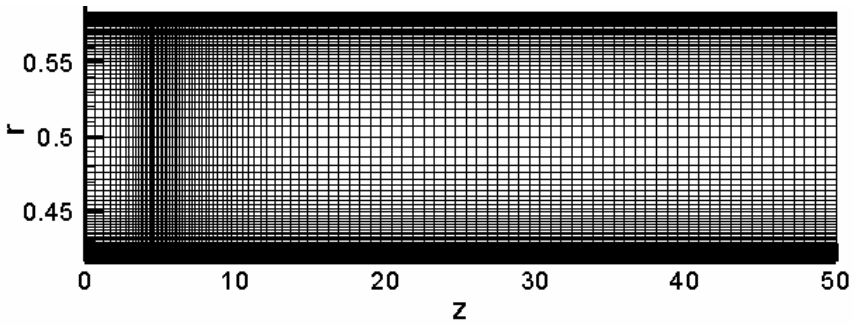

Figure 12: Computational grid for concentric cylinder test case

Similar to a pipe, fully developed flow in the annular space between two concentric cylinders presents an ideal verification case due to the simplifications and thereby direct analytical solution of the Navier-Stokes equations. For brevity, the analytical equation for the laminar flow velocity profile between concentric cylinders is:

Equation 56: Axial Velocity Distribution for Laminar Flow through Concentric Cylinders

$$u(r) = \left(-\frac{\partial p}{\partial x}\right)\frac{1}{4\mu}\left(r_{\max}{}^2 - r^2 + \frac{r_{\max}{}^2 - r_{\min}{}^2}{\ln\left(r_{\min}/r_{\max}\right)}\ln\left(\frac{r_{\max}}{r}\right)\right)$$

Analysis of annular flow at a Reynolds number, based on hydraulic diameter ($D_h = 2(r_{max} - r_{min})$), of ~600 was performed. The computational domain, shown in Figure 12, is constructed with 105 axial and 81 radial points. Hyperbolic stretching in both the axial and radial directions resolves the inlet and viscous wall boundary layers, respectively. The upstream boundary is placed ~2.5 hydraulic diameters (D_h) preceding the concentric cylinder inlet. Again, the cylinder walls are considered to be adiabatic and the inlet total pressure and exit static pressure are held constant at ~20.15 N/m^2 (.424 lbs/ft^2) and ~20.15 N/m^2 (.421 lbs/ft^2), respectively. Assuming the top and bottom walls to be flat plates for boundary layer prediction, the Blasius laminar boundary layer equation, $\delta/z \approx 5.0/Re_z^{1/2}$, predicts an entrance length of ~0.503 m (1.65 ft). Therefore the concentric cylinders are modeled with a length of ~15.24 m (50 ft) to ensure fully developed flow. Similarly, using the entrance length equation for a pipe and substituting the hydraulic diameter for a conventional diameter, i.e. $L_e / D_h \approx 0.06Re_{Dh}$, the predicted entrance length is ~0.914 m (3.0 ft), which supports the previous choice of domain length.

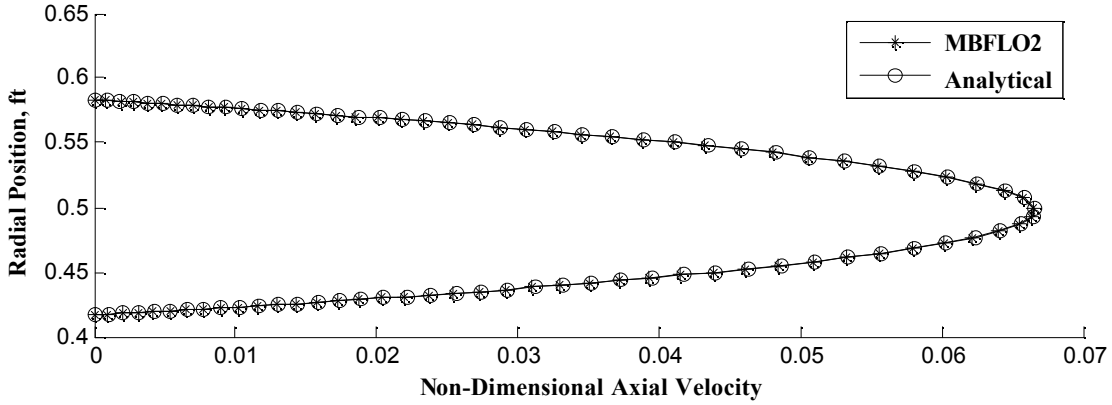

Figure 13: Numerical and Analytical axial velocity distributions for flow through concentric cylinders at Re_{Dh}~600, r_{outer}=.127m (7/12ft) and r_{inner}=.178m (5/12ft).

Analogous to laminar pipe flow, Figure 13 shows near equivalence between the numerically determined and analytically predicted velocity profiles. The maximum deviation between the numerical and analytical velocity profiles was again <0.10%. The contour plot, Figure 14, again

shows a nearly instantaneous boundary layer development, followed by a constant velocity profile, indicative of fully developed flow, throughout the remaining length of the annular space.

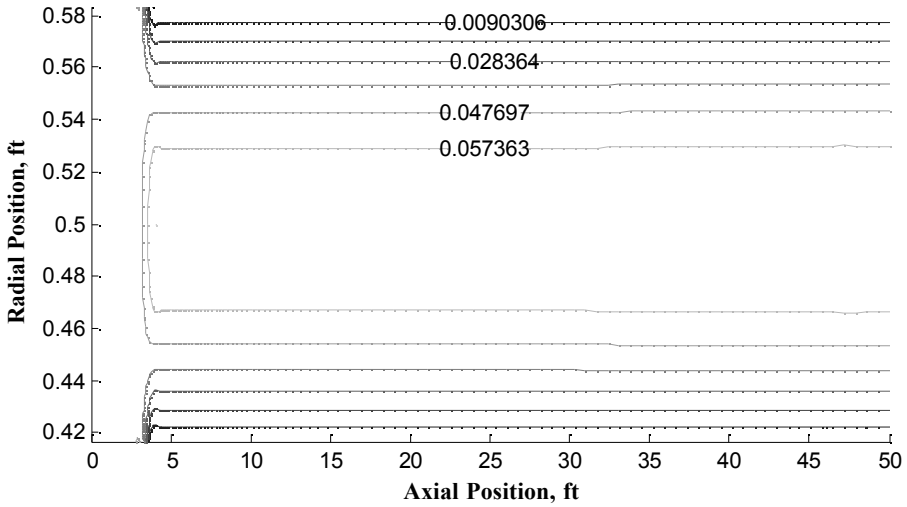

Figure 14: MBFLO2 axial velocity contours for laminar flow through concentric cylinders at Re_{Dh}~600, r_{outer}=.127m (7/12ft) and r_{inner}=.178m (5/12ft).

8.4 Turbulent Flow through Concentric Cylinders

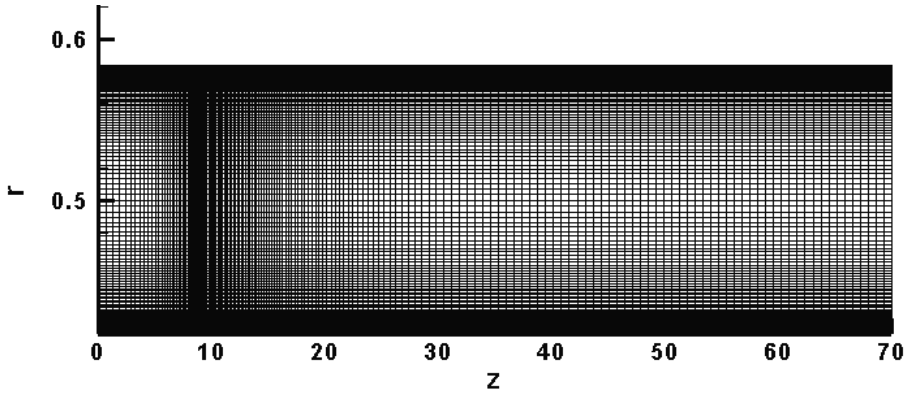

Figure 15: Computational grid for turbulent flow between concentric cylinders

By increasing the Reynolds number to ~33,333, based on hydraulic diameter ($D_h = 2(r_{max} - r_{min})$), analysis of turbulent flow between concentric cylinders was performed. The grid density of the laminar computational domain was increased to generate the grid shown in Figure 15, constructed of 168 axial and 113 radial points. Hyperbolic stretching resolves the inlet and viscous wall boundary layers. The upstream boundary is placed ~24 hydraulic diameters (D_h) preceding the concentric cylinder inlet. Again, the walls are considered to be adiabatic and the

inlet total pressure and exit static pressure are held constant at ~63105.62 N/m^2 (1327.88 lbs/ft^2) and ~59285.67 N/m^2 (1247.50 lbs/ft^2), respectively. Assuming the top and bottom walls to be flat plates for boundary layer prediction, the Blasius turbulent boundary layer equation, $\delta/z \approx 0.16/Re_z^{1/7}$, predicts an entrance length of ~0.97 m (3.18 ft), and therefore the concentric cylinders are modeled to have a length of ~19.202 m (63 ft) to ensure fully developed flow. Similarly, using the entrance length equation for turbulent pipe flow and utilizing the hydraulic diameter, i.e. $L_e / D_h \approx 4.4Re_{Dh}^{1/6}$, the predicted entrance length is ~1.13 m (3.7 ft), which supports the previous estimate.

For verification with a fully developed turbulent flow between concentric cylinders, logarithmic profiles from the inner and outer cylinder walls can be patch together to approximate the velocity profile. Similar to Equation 57, the following equation will provide the fully developed velocity profiles coming from the inner and outer cylinder walls:

Equation 57: Axial Velocity Distribution for Turbulent Pipe Flow

$$u(r_{i,o}) \approx \frac{u_{i,o}^{*}}{0.41} \ln\left(\frac{y u_{i,o}^{*}}{v} \right) + 5.0$$

where y is the distance from the cylinder wall and u^* is the friction velocity at both the inner and outer cylinder walls, defined by the law of the wall given below:

Equation 58: Law of the Wall

$$u_{i,o}^{*} = \left(\frac{\tau_{w_{i,o}}}{\rho} \right)^{1/2}$$

where τ_{w_i} is the inner wall shear stress and τ_{w_o} is the outer wall shear stress.

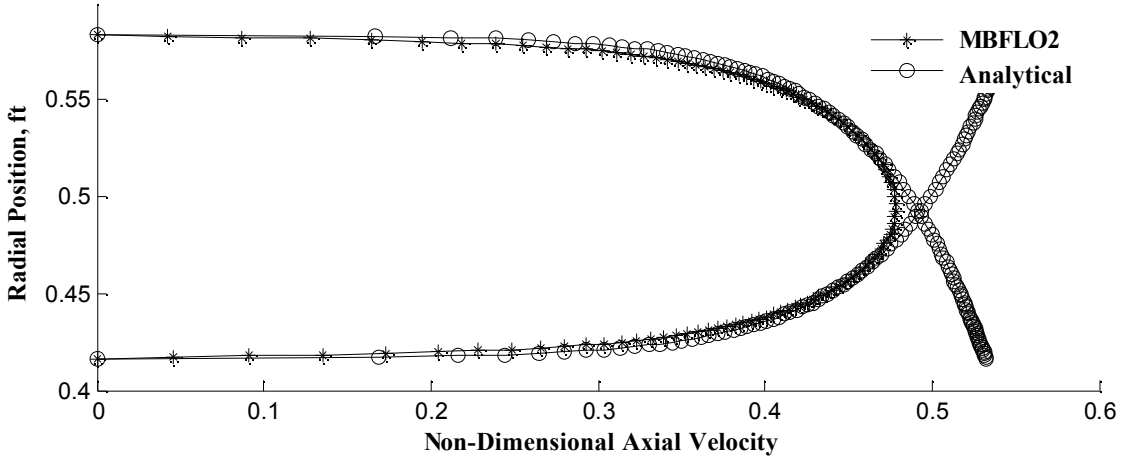

Figure 16: Numerical and Analytical axial velocity distributions for turbulent flow through concentric cylinders at $Re/_{Dh}$=100,000 1/L, r_{outer}=.127m (7/12ft) and r_{inner}=.178m (5/12ft).

Figure 16, plot of axial velocity distribution, shows that the analytical log-law profile, predicted from the inner and outer cylinder wall shear stress, closely encapsulates the numerically predicted velocity profile. As was seen for the laminar case, the log-law over predicts the transitional shear stress between the inner and overlap regions. Additionally, the log-law profile over predicts the maximum velocity because it does not accurately capture the shear stress at boundary layer interactions, i.e. along the flow centerline.

8.5 Rotating Wall Case Study

To complete the verification of the axisymmetric terms in the RANS code, rotational flow must be considered. For simplicity and direct analytical solution of the N-S equations, purely rotational flow between infinitely long concentric cylinders, inner cylinder stationary and outer cylinder rotating, is considered. The analytical equation for laminar flow between a stationary and rotating cylinder is:

Equation 59: Laminar Radial Velocity Distribution between Concentric Cylinders – Outer Cylinder Rotating

$$w(r) = \Omega r_o \left(\left(\frac{r_i}{r} - \frac{r}{r_i} \right) \Big/ \left(\frac{r_i}{r_o} - \frac{r_o}{r_i} \right) \right)$$

where r_i is the radius of the inner cylinder, r_o is the outer cylinder radius, Ω is the wall rotation rate (rad/s), and r is the radial position.

Analysis of laminar rotating flow between infinite concentric cylinders with the outer cylinder rotating was performed at three rotational rates to demonstrate the capability to analyze flows with and without strong rotation and to explore the numerical instabilities previously mentioned. The analysis was performed at rotation rates of 200, 400, and 1000 radians/sec, which at an outer radius (r_o) of 0.06m (~.197ft) correlates to 12 (39.37), 24 (78.74), and 60 m/s (196.85 ft/s). With a total temperature (T_t) of 300K (540R) and using the definition of Mach number along with the total-static Mach number relations, the corresponding wall Mach numbers are predicted as follows:

Equation 60: Rotational Mach Number Calculation

$$M^2 = \frac{V^2}{\gamma R T_s}$$

$$T_s = T_t\left(1+\frac{\gamma-1}{2}M^2\right)^{-1}$$

$$M^2\left(1+\frac{\gamma-1}{2}M^2\right) = \frac{V^2}{\gamma R T_t}$$

$$M^2 = \frac{-1+\sqrt{1+4\left(\frac{\gamma-1}{2}\right)\frac{V^2}{\gamma R T_t}}}{\gamma-1}$$

Thus, the wall rotational Mach numbers were predicted to be ~0.0346, ~0.0693, and ~0.1732 for the rotation rates of 200, 400, and 1000 rad/s respectively. Though all of the rotational Mach numbers are relatively small, numerical instabilities due to strong rotational source terms become apparent at rotation rates of ~500-600 rad/s, thus converged solutions at 200 and 400 rad/s were used as initial conditions for analysis at 1000 rad/s. This method of progressively increasing rotation rates was outlined in Section 6 (rotational numerical instabilities), and proven viable in the following results.

The computational domain is 81 x 81 uniformly distributed points in the axial and radial direction. The inner cylinder radius (r_i) was .024 m (~0.787 ft), which, along with the outer radius already given, provides a radial spacing of 4.5 x 10^{-4} m (1.48 x 10^{-3} ft). Since this case study does not have conventional boundary layer flow, the velocity gradients normal to the cylinder walls are weak and thus the radial spacing is more than sufficient to resolve the flow characteristics. The radial boundaries corresponding to the cylinder walls are modeled with

adiabatic no-slip conditions and the axial boundaries are periodic (modeled as if attached to one another) to represent an infinite span.

For the first test case, rotation rate of 200 rad/s and Re/d = 5000 1/L, the numerical solution of rotational velocity (w(r)) was found to be identical to the analytical equation; shown in Figure 17.

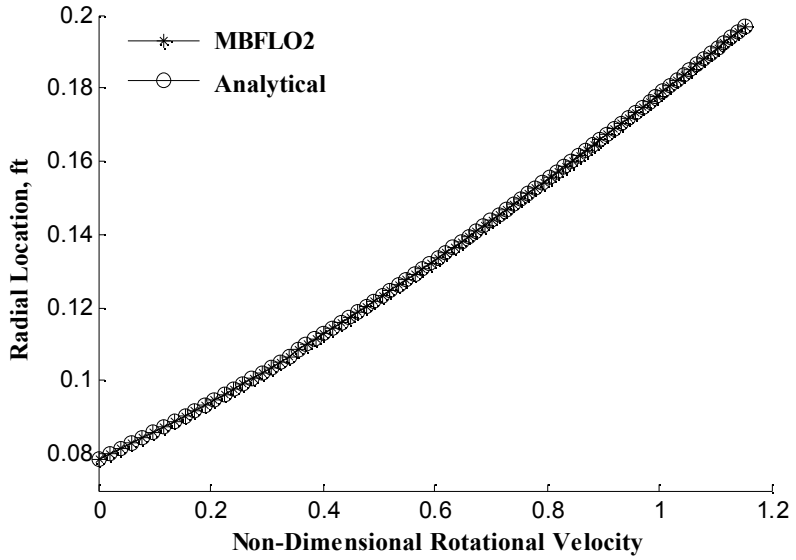

Figure 17: Numerical and Analytical rotational (theta) velocity distributions for flow within concentric cylinders with the outer wall rotating; Ω=200 rad/s. and Re/d= 5000 1/L.

This exact correlation to analytical theory verifies the correct solution of the rotational terms within the RANS equations. In addition, a visually accurate density distribution allows sign (or magnitude directionality) verification of the rotational terms and gives general insight to the rotation rate.

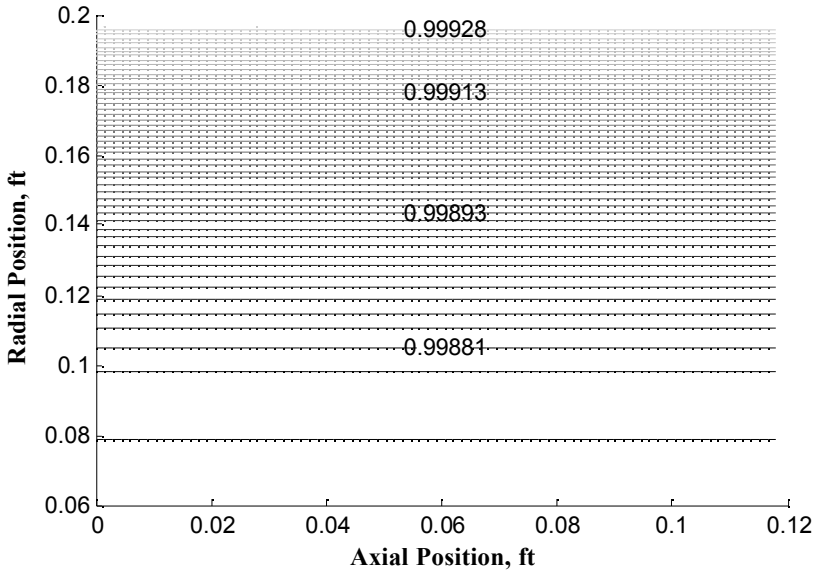

Figure 18: Numerical density contours for flow within concentric cylinders with the outer wall rotating; Ω=200 rad/s. and Re/d= 5000 1/L.

Figure 18 gives the line contours of density and as can be seen, the density is greatest along the outer wall, which is expected due to the Coriolis and centrifugal forces; proving the sign of the rotational source terms to be correct. Additionally, the small radial variation in density magnitude signifies a low rotation rate.

For brevity and to avoid the presentation of repetitious data, the case study results for a rotational rate of 400 rad/s are excluded. Again, the numerical and experimental radial distributions of rotational velocity coincided exactly. This test case was only necessary to obtain better flow profiles for an initial guess when numerically analyzing a rotational rate of 1000 rad/s.

The final rotational test case, performed at 1000 rad/s, presented several numerical instabilities as mentioned in Section 6. Initializing the flow field with constant pressure, density, and energy quickly led to a coupled divergence of the rotational source terms. This required the flow field to be initialized from a previously converged solution at a lower rotation rate (i.e. 400 rad/s), because it provided the radial dependence in the pressure, density, and energy profiles; though at incorrect magnitudes and distributions. For analysis, the wall rotation rate would then be instantaneously increased from the rate in the converged solution to the desired rate and the solution could then be iteratively solved for. The instantaneous velocity increase is undesirable numerically because it introduces discontinuities, but under small rotational changes, the viscous

stress terms quickly smooth the discontinuous flow variables. Rather than discontinuously changing rotation rate, allowing gradual increases in Ω with iterations and convergence would provide a better methodology and should be considered for further research in rotating flows.

In addition to using the flow solutions from a rotation rate of 400 rad/s, the axial momentum equation was ignored to prevent large scale decoupling as explained previously. Exclusion of the axial momentum equation was acceptable for this case study because the simplified N-S equations used to determine the analytical solution showed that the axial momentum was decoupled from the other variables. Therefore, by ignoring the axial momentum equation, initial convergence was obtain relatively quickly and provided a more sufficient prediction to the flow variables, which proved, in this case, to be viable initial conditions for solving the full set of momentum equations. The following numerical results for Ω = 1000 rad/s were then obtained by including the axial momentum equation and utilizing the initial solutions as a starting point:

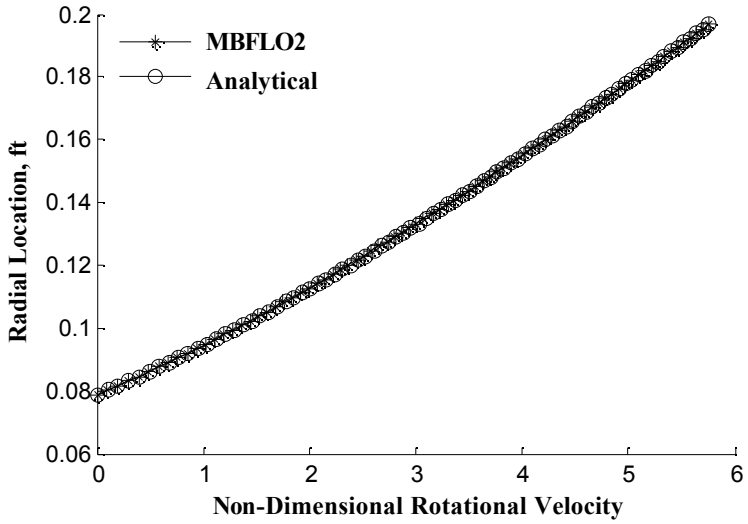

Figure 19: Numerical and Analytical rotational (theta) velocity distributions for flow between concentric cylinders with the outer wall rotating; Ω=1000 rad/s. and Re/d= 5000 1/L.

As for the first two rotation rates, Figure 19 shows the numerical and analytical radial distributions of rotational velocity to be nearly equivalent. Figure 20 provides a better depiction of the disparity between the analytical and numerical velocity distributions.

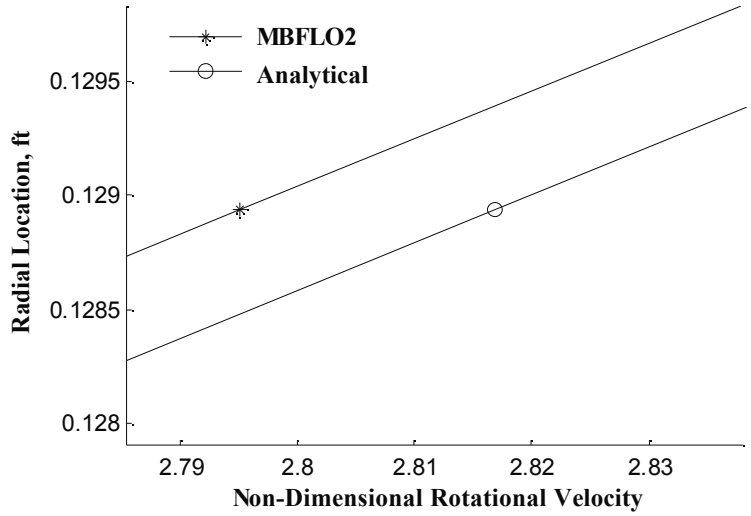

Figure 20: Error of Numerical rotational (theta) velocity distribution for flow between concentric cylinders with the outer wall rotating; Ω=1000 rad/s. and Re/d= 5000 1/L.

As can be seen in Figure 20, the maximum numerical error is <1.0%, which can be attributed to minimal convergence. Further iterations would improve convergence and thereby reduce error, but the computational efficiency to reduce the error beyond 1.0% is low. Finally, Figure 21 shows line contours for density and in comparison to Figure 18, there is a reasonable radial variation in density, which highlights the density-related physics and numerical issues as rotation rates increase. Some turbomachinery systems can have rotational rates above 100,000 rad/s, which quickly present regions of non-continuum gas and severally increase numerical complexity.

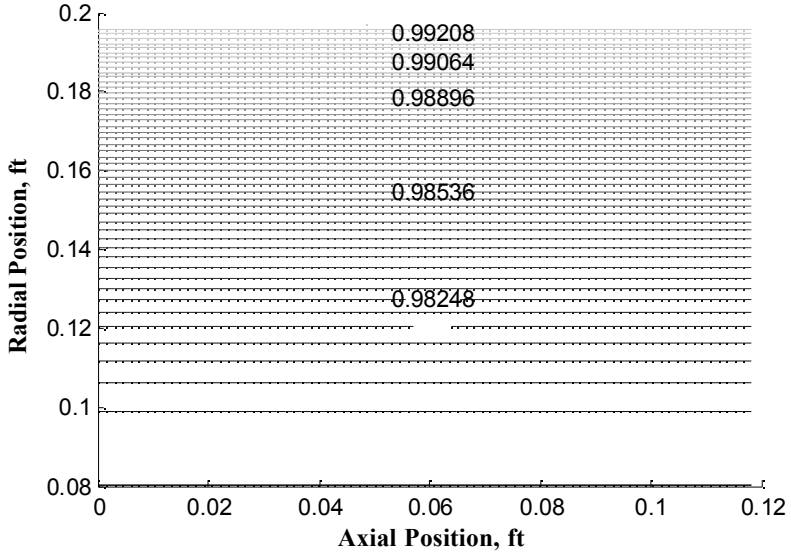

Figure 21: Numerical density contours for flow within concentric cylinders with the outer wall rotating; Ω=1000 rad/s. and Re/d= 5000 1/L.

8.6 Bachalo-Johnson Case Study

For validation with experimental data, analysis of transonic flow over an axial cylinder with an axisymmetric bump was performed and compared to experimental data presented by Bachalo and Johnson[20]. Exposed to the axisymmetric bump is a fully turbulent flow with a freestream Mach number of 0.875 and a unit Reynolds number Re/m = 13.6 x 10^6/m (41.45 x 10^6/ft). The cylinder has a 15.2 cm (0.5 ft) outer-diameter that extends 61 cm (2 ft) upstream of the bump, which has a thickness of 1.9 cm (0.062 ft) and chord length of 20.3 cm (0.67 ft). Additionally, the cylinder transitions smoothly into the bump via an 18.3 cm (0.6 ft) arc radius that is tangent to the bump and cylinder at 2.05 cm (0.067 ft) downstream and 3.33 cm (0.11 ft) upstream of the bump leading edge, respectively. The boundary conditions are comprised of an adiabatic solid viscous bump and cylinder, and a flow temperature of 294.4 K (530 R). Both the upper and exit boundaries allow for undisturbed outflow.

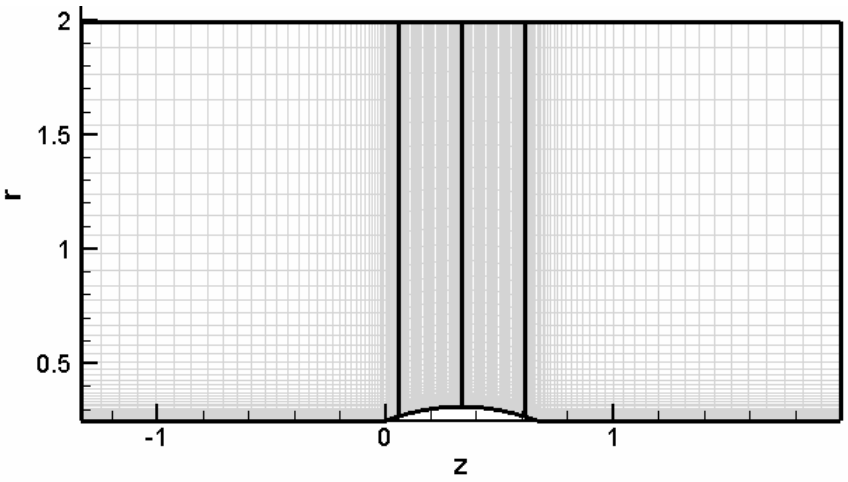

Figure 22: Multi-block axisymmetric bump setup.

Three numerical analyses, RANS (Reynolds-averaged Navier-Stokes), URANS (Unsteady Reynolds-averaged Navier-Stokes), and DES (detached-eddy simulation), along with a grid refinement study were performed on two multi-block grids composed of four blocks as generally displayed in Figure 22. The coarsest of the grids, shown in Figure 23, has four blocks comprised on 41 axial and 73 radial points (11972 total points).

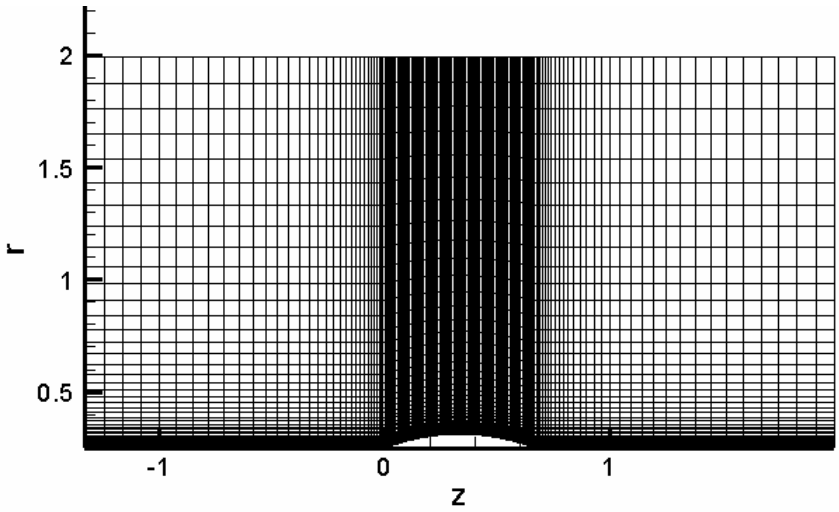

Figure 23: Multi-block axisymmetric bump grid 1.

The grid spacing normal to the viscous boundary, adjacent to the cylinder and bump, is 1.036 x 10^{-5} m (3.4 x 10^{-5} ft), while the axial spacing at the leading edge, across the bump, and at the trailing edge of the bump is 2.104 x 10^{-3} m (6.9 x 10^{-3} ft). Increasing the grid density, the fine grid shown in Figure 24 is comprised of four 81 x 145 point blocks (46,980 total points) with a normal wall spacing of 5.18 x 10^{-6} m (1.7 x 10^{-5}) and an axial bump spacing of 1.052 x 10^{-3} m (3.45 x 10^{-3} ft).

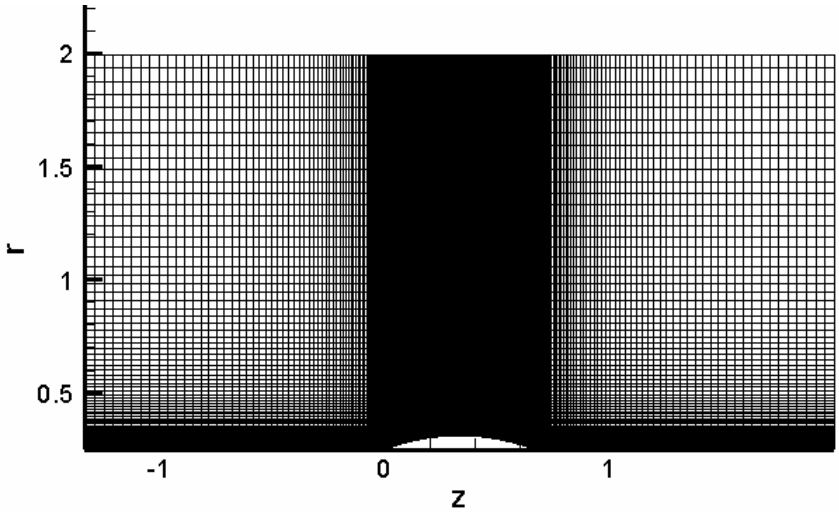

Figure 24: Multi-block axisymmetric bump grid 2

Hyperbolic grid stretching in the radial direction is utilized for accurately resolving the turbulent boundary layer, while in the axial direction, stretching is used for accurate computation of the shock and flow separation over the bump. The computation was performed in parallel using 4 processors. The steady RANS, URANS, and DES results are presented in the following sections.

8.6.1 Steady RANS Results

The steady RANS calculations were performed solving the Navier-Stokes equations with local time-steps and multi-grid acceleration to provide efficient convergence and steady state flow solutions. In 105,000 iterations for grid 1, the primary variable residuals were all significantly below 10^{-5}, thus suggesting adequate convergence. Comparing results to those given by Bachalo and Johnson[20], the surface static-to-total pressure ratios are plotted in Figure 25 for the experimental and numerical results.

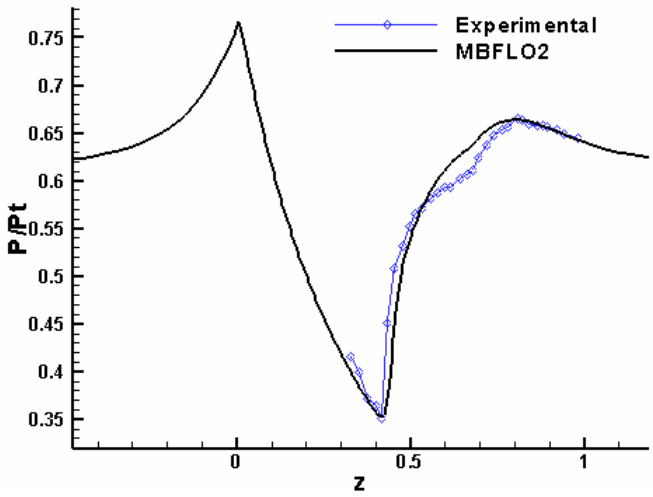

Figure 25: Experimental and numerical (RANS) total-to-static surface pressure distributions on grid 1.

Figure 25 shows the RANS capability, with use of the Ni/Lax-Wendroff scheme, to capture the shock location and to predict the pressure recovery. The discrepancy between the experimental and predicted results after the shock and before the full pressure recovery is attributed to the fact that the computation grid (Figure 23) does not include the fillet between the cylinder wall and the bump, thus a discontinuity in the flow surface at the trailing edge causes a quicker and more prominent pressure recovery.

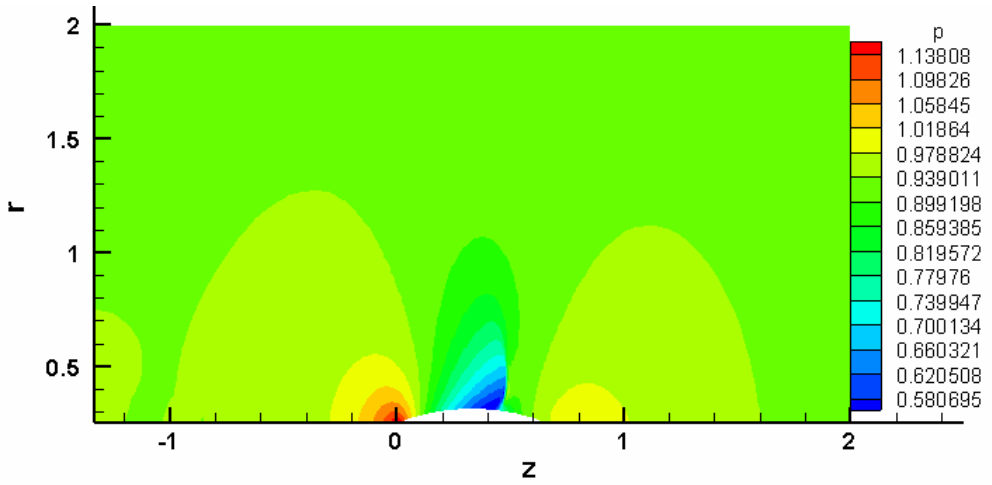

Figure 26: RANS pressure contours on grid 1.

Corresponding to the pressure ratio, Figure 26 gives the static pressure contours to further illustrate the flow over the axisymmetric bump. As shown, the leading edge discontinuity generates a high pressure region corresponding to a stagnation point. Then over the bump, the flow accelerates through a reduction in pressure, until the pressure gradient becomes too large on the back side of the bump and a shock generates to recover the pressure. At the trailing edge, there is another slight pressure increase due to the surface discontinuity.

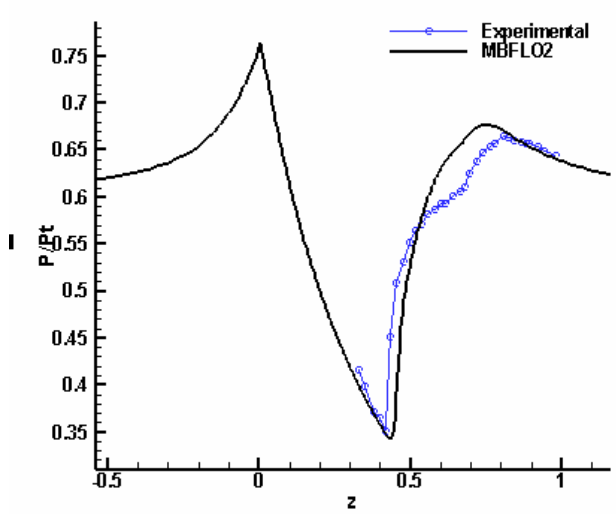

Figure 27: Experimental and numerical total-to-static surface pressure distributions on grid 2.

Increasing grid density, Figure 27 shows the total-to-static pressure ratio over the axisymmetric bump corresponding to grid 2 (Figure 24). Again, an accurate prediction of the shock location is provided, but the numerical total-to-static pressure ratio is slightly lower than

experimentally determined. Additionally, the pressure recovery following the shock occurs more rapidly, suggesting a stronger shock. The accelerated pressure recovery may be an effect of the increased trailing edge pressure caused by the surface discontinuity though.

8.6.2 Unsteady RANS (URANS) Results

For unsteady (URANS) and detached-eddy (DES) analysis, the unsteady behavior of the flow field must be analyzed and thus the simulations must be time accurate in order to capture the effects of self-excited flow. In both analyses, an unsteady dual time-step point implicit scheme is used to provide instantaneous results and a time-averaging scheme is used to represent bulk unsteady flow properties. Referring to the general form of the N-S equations, in Equation 34, the dual time-step scheme is a two-level iterative method which converges on a pseudo-time flux at each time-step until the time accurate solution is resolved; shown below:

Equation 61: Dual Time Step Scheme

$$\frac{\partial U}{\partial \tau} = -\frac{\partial U}{\partial t} - \frac{\partial (F)}{\partial x} - \frac{1}{r}\frac{\partial (rG)}{\partial r}$$

$$\frac{\partial U}{\partial t} = \frac{\Delta U}{\Delta t} = \frac{U^{n-2} - 4U^{n-1} + 3U^{n}}{2\Delta t}$$

where τ is pseudo-time.

As shown in Equation 61, the time accurate temporal derivative is moved to the right hand side of the equation and represented as a second order backward difference. Having the time-accurate temporal difference included in the current changes, i.e. U^{n}, the scheme becomes point implicit and allows the physical time step size, Δt, to be as large as desired.

Replacing the time accurate derivative on the left hand side of the equation with a pseudo-temporal flux term introduces an intermediate iteration, which must occur between each time accurate step, i.e. interval of Δt. The pseudo-time, τ, is not required to be constant because the pseudo-temporal flux reduces to zero as the time-accurate solution is approached. Basically, each time-accurate interval requires the steady-state solution of the pseudo-fluxes, thus during the inner iteration local pseudo-time-steps and multi-grid acceleration, which are not time accurate, can be used to accelerate convergence.

For unsteady flows, the oscillation dynamics control the shedding frequency around bluff bodies. Thus to accurately predict vortex shedding and eddies in the wake of the bump, a

Strouhal number of 0.2 is initially assumed to determine an acceptable time-step size capable of capturing the flow unsteadiness. The Strouhal number is defined as follows:

Equation 62: Strouhal Parameter $$St = \frac{\omega L}{U}$$

where ω is the oscillation (or shedding) frequency, L is the fundamental length scale, and U is the freestream velocity.

With a Strouhal number of 0.2, a trailing edge velocity of 280.26 m/s (919.5 ft/s), which assumes complete flow recovery at the bump trailing edge and corresponds to a Mach number of 0.875 and total temperature of 294.4 K (530R - inlet conditions), and a fundamental length scale of ~0.19 m (~0.0623 ft - bump height), Equation 62 provides a shedding frequency of 2951.98 1/s. By inverting the shedding frequency, the time of one shedding cycle is approximately 0.000339s. To capture moderate detail of the unsteady shedding of vortices, the physical time-step is then taken to be 1/100th of the shedding cycle or 3.4 x 10^{-6}s. In addition, the analysis is run for 40 shedding cycles to generate an accurate representation of the instantaneous flow. The analysis is then run for 40 additional cycles during which the flow is time-averaged.

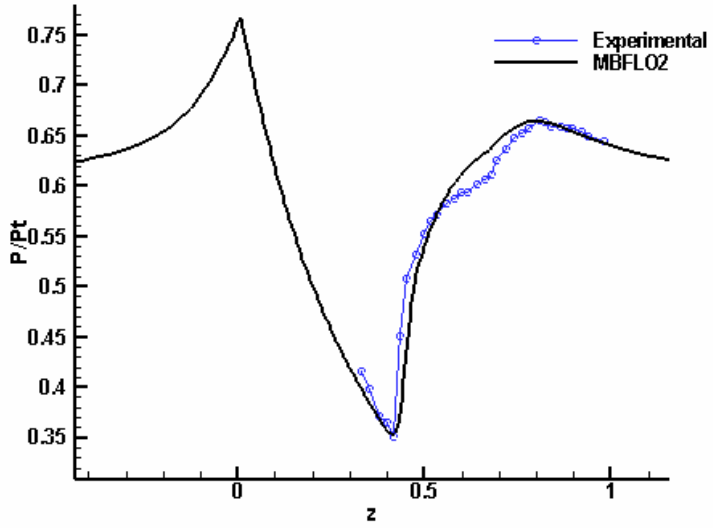

Figure 28: Experimental and time-averaged numerical (URANS) total-to-static surface pressure distributions on grid 1.

Figure 28 shows the numerical, URANS corresponding to grid 1, and experimental time-averaged total-to-static surface pressure distribution. The time-averaged unsteady surface

pressure distribution for the course grid shows no changes when compared to the RANS results. The shock location is still accurately predicted and the resolution of vortex shedding is not apparent due to the damping of the k-ω turbulence equations.

Figure 29 presents the numerical time-averaged pressure contours, which in comparison to Figure 26 shows that the URANS solution is comparable to the RANS solution.

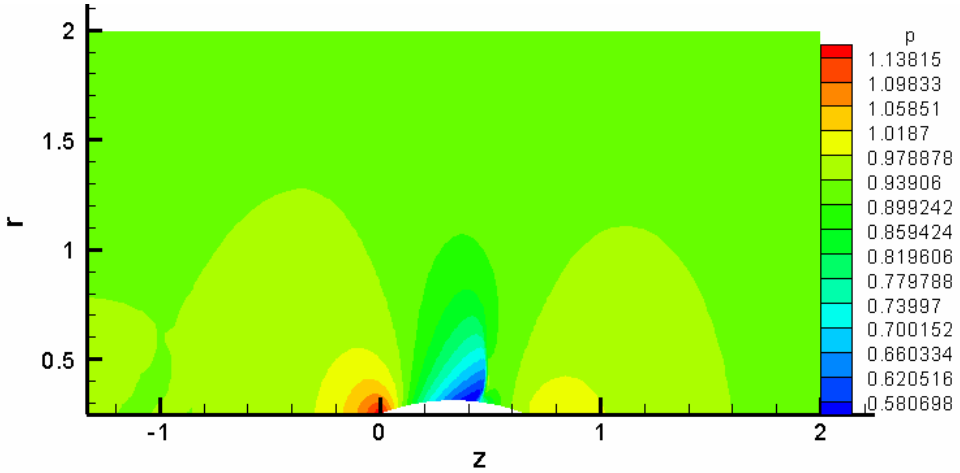

Figure 29: Numerical (URANS) time-averaged pressure contours on grid 1.

Moving to the finer grid, the URANS total-to-static surface pressure distribution, shown in Figure 30, still presents stable results that do not indicate unsteadiness or vortex shedding.

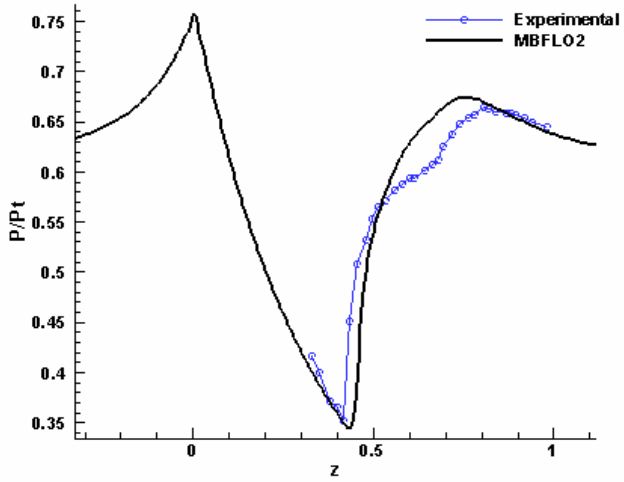

Figure 30: Experimental and time-averaged numerical (URANS) total-to-static surface pressure distributions on grid 2.

From these results it is reasonable to presume that time-accurate Reynolds-averaged solutions are unnecessary since URANS simulations do not indicate vortex shedding or any form of unsteady wake phenomena for either the course or fine grids.

8.6.3 DES Results

Before presenting and interpreting the detached-eddy simulation results, an annotation of the current state of DES research is given. Currently, research into DES predictions of shock boundary layer interaction is limited and often substandard at best. More specifically, the turbulence modeled in regions of large turbulence length scale of detached-eddy simulations is proportional to the computational grid spacing and the C_{des} scaling coefficient described in Eqs. 24 and 25. Suggested values for the C_{des} coefficient in various applications shown in the open literature range from 0.1 to 0.8. The larger the C_{des} value, the more dissipation is added to the turbulent kinetic energy equation (Equation 21) as given by Equation 25. In the current simulations, the value of the C_{des} coefficient was 0.65. The results to be shown below seem to indicate that the flow field resulting from the detached-eddy simulation is too laminar-like, indicating that the C_{des} coefficient is too large. Since detached-eddy simulations have never previously been performed for axisymmetric configurations, this simulation provides important data for the eventual calibration of the C_{des} coefficient for these flows. Further simulations and comparison with experimental data are required to improve the accuracy of these simulations.

Mindful of the note toward DES capabilities and using the computational methods outlined in the previous section, the time-averaged DES total-to-static surface pressure distribution results for the course grid are presented in Figure 31. As expected, the results are distinctly different from those obtained from RANS and URANS calculations. The pressure generation along the leading edge of the bump corresponds well with the RANS, URANS, and experimental data, but the shock location, strength, and pressure distribution over the bump are contradictory to the other data. Realizing the probable insufficiency of the DES length scaling, interpretation of the pressure distribution may be fruitless. Even so, Figure 31 suggests vortex shedding in which a shock develops, as shown from the RANS and URANS results, and due to the unsteadiness of the shock/boundary layer interaction, the viscous flow downstream of the shock breaks down into trailing vortices. The viscous flow breakdown results in a weaker shock more toward the leading edge of the bump, and a pressure sink aft of the trailing edge, which indicates a trailing vortex.

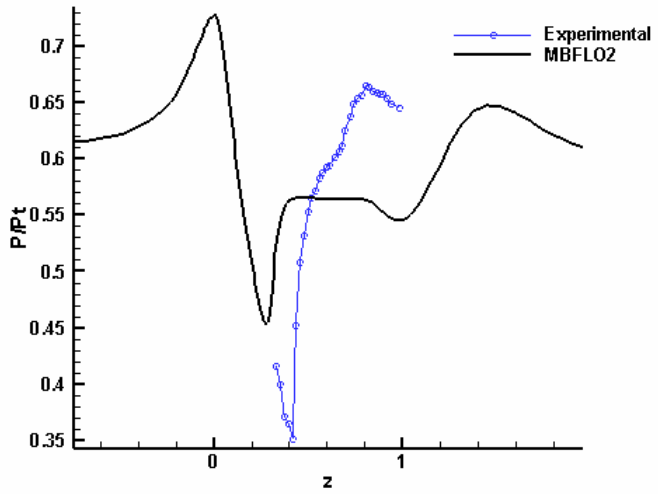

Figure 31: Experimental and numerical (time-averaged DES) total-to-static surface pressure distributions on grid 1.

Figure 32 provides the corresponding Mach number contours for the grid 1 results and shows the increased region of separated flow behind the axisymmetric bump. The increased region of separated flow, which detaches from the bump apex, is indicative of laminar flow, which has a limited ability to remain attached to a surface through adverse pressure gradients. Turbulent flow on the other hand, resists flow separation in adverse pressure gradients as shown in the RANS and URANS results. Therefore, the results suggest that the value of C_{des} should be considerably less than 0.65 to accurately predict the shock location, flow separation point, and unsteady phenomena.

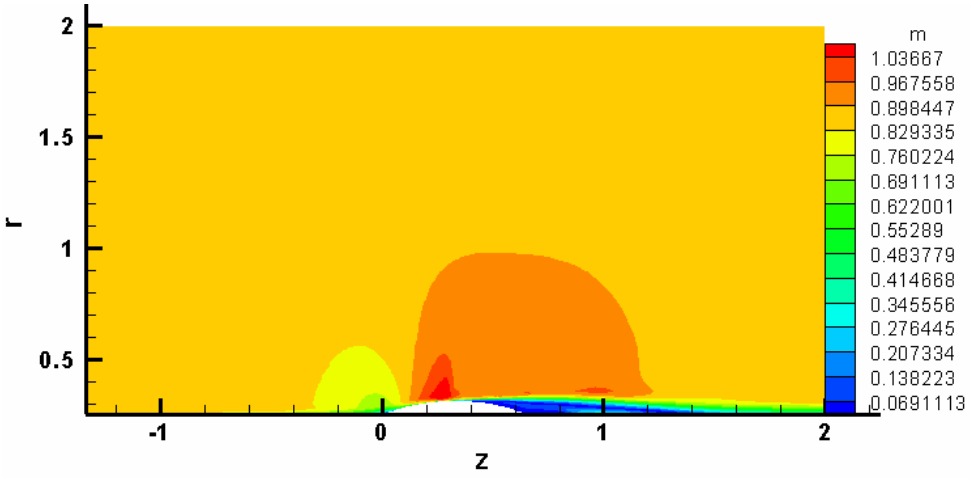

Figure 32: Numerical (DES) time-averaged Mach contours on grid 1.

Moving to the course grid, similar results are shown in Figures 33 and 34 for the surface total-to-static pressure ratio and the Mach number contours, respectively. In the wake region, the increased grid density does resolve more unsteady flow phenomena, but vortex shedding is still not captured correctly to any distinguishable degree.

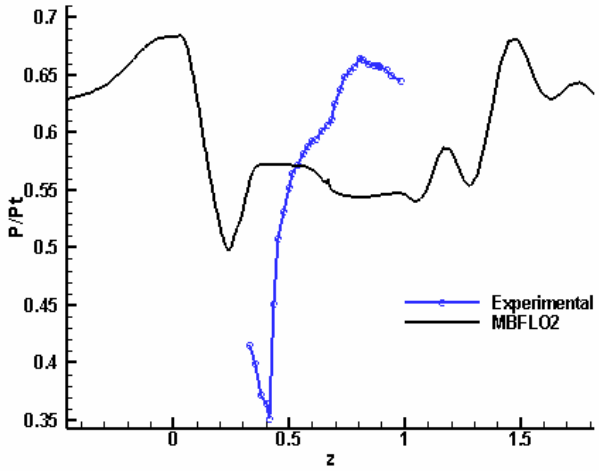

Figure 33: Experimental and numerical (time-averaged DES) total-to-static surface pressure distributions on grid 2.

The Mach number contours show that the fine grid captures a significantly longer wake region generated from a flow separation point predicted further forward on the bump, again suggesting the inadequacy of the current C_{des} value.

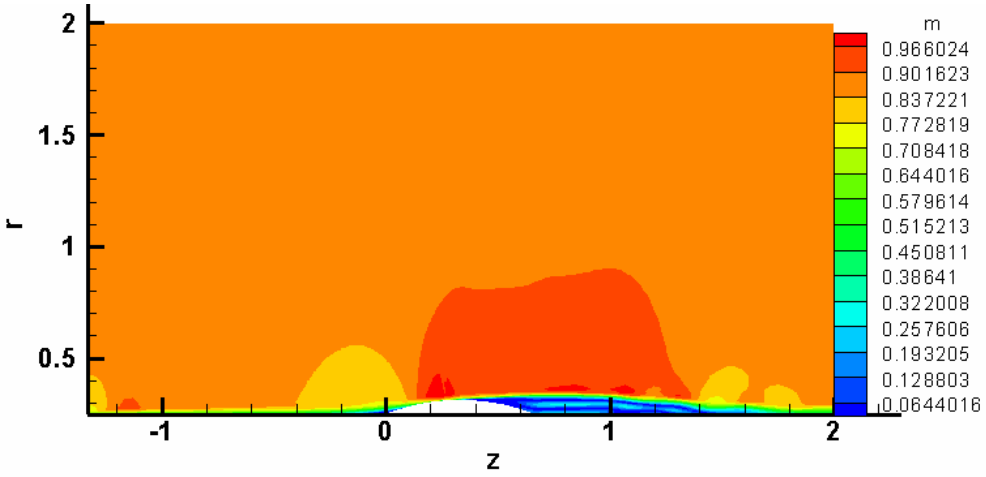

Figure 34: Numerical (DES) time-averaged Mach contours on grid 2

In general, the RANS and URANS calculations accurately predict a steady flow over the axisymmetric bump. The shock location, surface pressure distribution, and flow separation point

correspond strongly with experimental data. Conversely, current detached-eddy simulations are unable to predict the shock boundary layer interactions and thus present nearly laminar results, which suggest the necessity to further research the turbulent length scaling coefficients; in particular C_{des}.

8.7 Centrifuge Case Study (Future Research)

Preparation for accurate steady and unsteady RANS/DES analysis of flow within an axial centrifuge is being conducted. Figure 35 shows a current 9 block grid setup that captures both the inlet and exit boundaries within individual blocks to allow either inflow/outflow or prescribed mass-flow transpiration boundary conditions. The inner radius wall will be modeled as a slip boundary condition due to the non-continuum flow conditions, while the side walls and outer radius are no slip boundaries. Inflow and outflow boundaries will be controlled by setting the mass flow rates in accordance with measured values. The mean flow temperature (T_{mean}) will be set to 300 K and the outer radial wall will have a linear temperature gradient which varies from $0.95T_{mean}$ to $1.05T_{mean}$ between z_{min} and z_{max}, respectively.

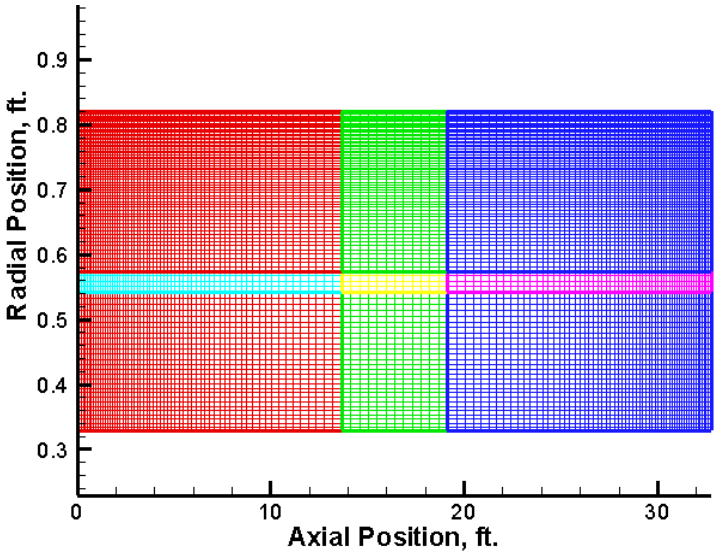

Figure 35: Multi-block centrifuge grid.

The analysis goals will be to accurately resolve the Ekman layers, radial density profiles, and counter-flow characteristics.

9 Conclusion

An extended second-order finite volume integration method and two equation k-ω turbulence model for analysis of internal/external axisymmetric flows with and without strong rotation has been presented. The Lax-Wendroff/Ni distribution formulae have been extended to accurately account for grid stretching and cylindrical coordinates. This has been accomplished by preserving the piecewise integration and distribution of the temporal changes to the flow variables, while maintaining accuracy and computational efficiency. Accuracy is demonstrated through verification with laminar and turbulent pipe, concentric cylinder flow, and rotating concentric cylinder flow test cases. Validation against experimental data for a transonic bump with separated flow has also been performed.

Appendix A: Expansion of Second Order Temporal Integration Equation

$$\frac{\Delta t^2}{2}\frac{\partial^2 U}{\partial t^2}\bigg|_{i,j} = \frac{\Delta t}{2V_{i,j}}\left[\begin{array}{l}
\frac{1}{4}\Delta F_{i-\frac{1}{2},j-\frac{1}{2}}\left(\left(r_{i+\frac{1}{2},j-\frac{1}{2}}-r_{i-\frac{1}{2},j-\frac{1}{2}}\right)\left(r_{i+\frac{1}{2},j-\frac{1}{2}}+r_{i-\frac{1}{2},j-\frac{1}{2}}\right)-\left(r_{i-\frac{1}{2},j+\frac{1}{2}}-r_{i-\frac{1}{2},j-\frac{1}{2}}\right)\left(r_{i-\frac{1}{2},j+\frac{1}{2}}+r_{i-\frac{1}{2},j-\frac{1}{2}}\right)\right)+\\
\frac{1}{4}\Delta F_{i+\frac{1}{2},j-\frac{1}{2}}\left(\left(r_{i+\frac{1}{2},j-\frac{1}{2}}-r_{i-\frac{1}{2},j-\frac{1}{2}}\right)\left(r_{i+\frac{1}{2},j-\frac{1}{2}}+r_{i-\frac{1}{2},j-\frac{1}{2}}\right)+\left(r_{i+\frac{1}{2},j+\frac{1}{2}}-r_{i+\frac{1}{2},j-\frac{1}{2}}\right)\left(r_{i+\frac{1}{2},j+\frac{1}{2}}+r_{i+\frac{1}{2},j-\frac{1}{2}}\right)\right)+\\
\frac{1}{4}\Delta F_{i+\frac{1}{2},j+\frac{1}{2}}\left(\left(r_{i+\frac{1}{2},j+\frac{1}{2}}-r_{i+\frac{1}{2},j-\frac{1}{2}}\right)\left(r_{i+\frac{1}{2},j+\frac{1}{2}}+r_{i+\frac{1}{2},j-\frac{1}{2}}\right)-\left(r_{i-\frac{1}{2},j+\frac{1}{2}}-r_{i+\frac{1}{2},j+\frac{1}{2}}\right)\left(r_{i-\frac{1}{2},j+\frac{1}{2}}+r_{i+\frac{1}{2},j+\frac{1}{2}}\right)\right)+\\
\frac{1}{4}\Delta F_{i-\frac{1}{2},j+\frac{1}{2}}\left(-\left(r_{i-\frac{1}{2},j+\frac{1}{2}}-r_{i+\frac{1}{2},j+\frac{1}{2}}\right)\left(r_{i-\frac{1}{2},j+\frac{1}{2}}+r_{i+\frac{1}{2},j+\frac{1}{2}}\right)-\left(r_{i-\frac{1}{2},j+\frac{1}{2}}-r_{i-\frac{1}{2},j-\frac{1}{2}}\right)\left(r_{i-\frac{1}{2},j+\frac{1}{2}}+r_{i-\frac{1}{2},j-\frac{1}{2}}\right)\right)+\\
\frac{1}{4}\Delta G_{i-\frac{1}{2},j-\frac{1}{2}}\left(-\left(z_{i+\frac{1}{2},j-\frac{1}{2}}-z_{i-\frac{1}{2},j-\frac{1}{2}}\right)\left(r_{i+\frac{1}{2},j-\frac{1}{2}}+r_{i-\frac{1}{2},j-\frac{1}{2}}\right)+\left(z_{i-\frac{1}{2},j+\frac{1}{2}}-z_{i-\frac{1}{2},j-\frac{1}{2}}\right)\left(r_{i-\frac{1}{2},j+\frac{1}{2}}+r_{i-\frac{1}{2},j-\frac{1}{2}}\right)\right)+\\
\frac{1}{4}\Delta G_{i+\frac{1}{2},j-\frac{1}{2}}\left(-\left(z_{i+\frac{1}{2},j-\frac{1}{2}}-z_{i-\frac{1}{2},j-\frac{1}{2}}\right)\left(r_{i+\frac{1}{2},j-\frac{1}{2}}+r_{i-\frac{1}{2},j-\frac{1}{2}}\right)-\left(z_{i+\frac{1}{2},j+\frac{1}{2}}-z_{i+\frac{1}{2},j-\frac{1}{2}}\right)\left(r_{i+\frac{1}{2},j+\frac{1}{2}}+r_{i+\frac{1}{2},j-\frac{1}{2}}\right)\right)+\\
\frac{1}{4}\Delta G_{i+\frac{1}{2},j+\frac{1}{2}}\left(-\left(z_{i+\frac{1}{2},j+\frac{1}{2}}-z_{i+\frac{1}{2},j-\frac{1}{2}}\right)\left(r_{i+\frac{1}{2},j+\frac{1}{2}}+r_{i+\frac{1}{2},j-\frac{1}{2}}\right)+\left(z_{i-\frac{1}{2},j+\frac{1}{2}}-z_{i+\frac{1}{2},j+\frac{1}{2}}\right)\left(r_{i-\frac{1}{2},j+\frac{1}{2}}+r_{i+\frac{1}{2},j+\frac{1}{2}}\right)\right)+\\
\frac{1}{4}\Delta G_{i-\frac{1}{2},j+\frac{1}{2}}\left(\left(z_{i-\frac{1}{2},j+\frac{1}{2}}-z_{i+\frac{1}{2},j+\frac{1}{2}}\right)\left(r_{i-\frac{1}{2},j+\frac{1}{2}}+r_{i+\frac{1}{2},j+\frac{1}{2}}\right)+\left(z_{i-\frac{1}{2},j+\frac{1}{2}}-z_{i-\frac{1}{2},j-\frac{1}{2}}\right)\left(r_{i-\frac{1}{2},j+\frac{1}{2}}+r_{i-\frac{1}{2},j-\frac{1}{2}}\right)\right)
\end{array}\right]$$

Work Cited

[1] Galperin, H. "Turbulence Model for Rotating Flows," *AIAA Journal*, Vol. 27, No. 6, 1989, pp. 750, 757.

[2] Koyama, Hide S., "Effects of Coriolis Force on Flow in Rotating Diffusers," *AIAA Journal*, Vol. 35, No. 7, 1997, pp. 1164, 1170.

[3] Tsunetoshi, Kai. "Designing and Analysis Study of Uranium Enrichment with Gas Centrifuge." Japan. Proceedings to *The 9th International Workshop on Separation Phenomena in Liquids and Gases*. September 18-21, 2006. Beijing, China.

[4] Wilcox, D. C., "Reassessment of the Scale-Determining Equation for Advanced Turbulence Models," *AIAA Journal*, Vol. 26, No. 11, 1988, pp. 1299, 1310.

[5] Smagorinsky, J., "General Circulation Experiments with the Primitive Equations," *Mon. Weather Rev*., Vol., 91 pp. 99,164.

[6] Strelets, M., "Detached Eddy Simulation of Massively Separated Flows," AIAA 2001-879, January 2001.

[7] Bush, R. H. and Mani, M., "A Two-Equation Large Eddy Stress Model for High Sub-Grid Shear," AIAA 2001-2561, June 2001.

[8] Andrade, A., and Davis, R., "A RANS/DES Numerical Procedure for Axisymmetric Flows with and without Strong Rotation," *AIAA Reno Conference*, 2008.

[9] Ni, R. H., "A Multiple Grid Scheme for Solving the Euler Equations," *AIAA Journal*, Vol. 20, 1982, pp. 1565, 1571.

[10] Dannenhoffer, J. F., "Grid Adaptation for Complex Two-Dimensional Transonic Flows", CFDL-TR-87-10, Department of Aeronautics and Astronautics, Massachusetts Institute of Technology, August 1987.

[11] Davis, R. L., Ni, R. H., and Carter, J. E., "Cascade Viscous Flow Analysis Using The Navier-Stokes Equations," *AIAA Journal of Propulsion and Power*, Vol. 3, No. 5, September-October 1987.

[12] Davis, R. L., Hobbs, D. E., and Weingold, H. D., "Prediction of Compressor Cascade Performance Using a Navier-Stokes Technique", *ASME Journal of Turbomachinery*, Vol. 110, No. 4, pp. 520-531, 1988.

[13] Jameson, A., Schmidt, W., Turkel, E., "Numerical Solutions of the Euler Equations by Finite Volume Methods Using Runge-Kutta Time-Stepping Schemes," AIAA 81-1259, June 1981.

[14] Chima, R. V., "Analysis of Inviscid and Viscous Flows in Cascades with an Explicit Multiple-Grid Algorithm," *AIAA Journal of Propulsion and Power,* September-October, 1987.

[15] Sorenson, R. L., "A Computer Program to Generate Two-Dimensional Grids About Airfoils and Other Shaped by the Use of Poisson's Equation", NASA TM-81198.

[16] Thompson, J. F., Thames, F. C., and Mastin, C. W., "Automatic Numerical Grid Generation of Body-Fitted Curvilinear Coordinate System for Field containing Any Number of Arbitrary Two-Dimensional Bodies," *Journal of Computational Physics*, Vol. 15, No. 3, July 1974.

[17] MPI: A Message-Passing Interface Standard

[18] Davis, R., Alonso, JJ., Yao, J., Paolillo, R., Sharma, O.P. "Prediction of High-Pressure Turbine Main-/Secondary-Air System Flow Interaction," Journal of Propulsion and Power 21-1, January-February 2005.

[19] White, F. M. Fluid Mechanics. Fifth Edition, Mc Graw Hill, 2003.

[20] Bachalo, W.D., Johnson, D. A., "Comparison Between Experimental and Prediction for a Transonic Turbulent Separated Flow," *AIAA Journal*, Vol. 20, No. 6, June 1982.